

Physical parameters of stellar population in star formation regions of galaxies

A. S. Gusev¹,^{*} F. Sakhibov,² O. V. Egorov^{1,3}, V. S. Kostiuik⁴ and E. V. Shimanovskaya¹

¹*Sternberg Astronomical Institute, Lomonosov Moscow State University, Universitetsky pr. 13, Moscow 119234, Russia*

²*University of Applied Sciences, Technische Hochschule Mittelhessen, D-61169 Friedberg, Germany*

³*Astronomisches Rechen-Institut, Zentrum für Astronomie der Universität Heidelberg, Mönchhofstraße 12-14, D-69120 Heidelberg, Germany*

⁴*St. Petersburg State University, Universitetskaya nab. 7/9, St. Petersburg 199034, Russia*

Accepted 2023 July 7. Received 2023 July 6; in original form 2022 December 21

ABSTRACT

We present the results of a study of young unresolved stellar groupings (clusters, OB associations, and their complexes) associated with H II regions, based on the coupling of spectroscopic, photometric and H α spectrophotometric observations of star formation regions. Along with our own observations, we use a part of the spectroscopic and H α data from the literature and open data bases. The study is based on the catalogue of 1510 star formation regions with ages ~ 10 –20 Myr in 19 spiral galaxies, compiled by us earlier. We study the morphology of stellar groupings and their relation with the associated H α emission region. Extinctions, gas chemical abundances, and sizes of star formation regions are measured. Using numerical simple stellar population models computed for metallicities fixed from observations to intrinsic colours of the studied star formation regions, we estimated ages and masses of stellar population of 400 young stellar groupings. Different relations between observational and physical parameters of the young stellar population in star formation regions are discussed.

Key words: H II regions – galaxies: ISM – galaxies: star clusters: general – galaxies: star formation.

1 INTRODUCTION

To understand processes of modern star formation in galaxies and to study the early evolution of star clusters, OB associations and complexes, one needs to estimate physical and chemical parameters of young stellar groupings in star formation regions, including their age, mass, size, and metallicity. A galaxy star-forming region is a single mixture of newly formed star clusters, ionized gas, and clouds of molecular gas and dust. Star formation regions form a hierarchical structure on scales from a few to several hundreds of parsecs. The largest star formation regions are star complexes with typical sizes of about 300–700 pc (Elmegreen & Efremov 1996; Efremov & Elmegreen 1998). The diameters of the largest complexes reach 2 kpc (Elmegreen et al. 1996). These complexes are the largest coherent groupings of stars, clusters, and associations which are connected by the unity of the origin from the same H₂ supercloud (Efremov 1989, 1995; Elmegreen 1994, 2009; Odekon 2008; de la Fuente Marcos & de la Fuente Marcos 2009). On small scales, there are star clusters with sizes from a few parsecs which have been formed within dense cores of giant molecular clouds (GMCs). OB associations and stellar aggregates with sizes from ~ 40 to ~ 200 pc occupy intermediate scales of star formation.

This paper focuses on studying the stellar groupings in star formation regions of rather distant galaxies (see Table 1). The angular resolution of our observations ~ 1 –1.5 arcsec corresponds to the linear resolution 30–40 pc for the nearest galaxies NGC 628, NGC 5585, and NGC 6946, and 350–400 pc in the faraway galaxies

NGC 783 and IC 1525. It does not allow us to separate the young star clusters and OB associations even in the nearest galaxies: smaller star clusters are observed as star-like objects with diameters of 30–40 pc. In more distant galaxies, we can observe star formation regions with sizes of 200–300 pc and larger, i.e. star complexes. Star clusters, embedded in star formation regions, are dense aggregates of young stars, formed at essentially the same time in the same region of space (Portegies Zwart, McMillan & Gieles 2010). In our previous paper (Gusev et al. 2016), we found that the minimal masses of the studied star clusters in the nearest galaxies NGC 628 and NGC 6946 are $\approx 1 \times 10^4 M_{\odot}$. According to Portegies Zwart et al. (2010), star clusters that are more massive than $\sim 10^4 M_{\odot}$ are determined as young massive clusters. Gieles & Portegies Zwart (2011) showed that the youngest (age ≤ 10 Myr) clusters and associations are poorly separated. Thus, most of the objects studied here are young massive clusters (associations) or complexes of young star clusters. Hereinafter, we will call the studied stellar populations in star formation regions the ‘stellar groupings’. It shall be understood that this common term encompasses different types of young objects, from giant complexes of clusters and stars to OB associations and star clusters.

A star formation region goes through several stages of evolution during first tens Myr of its life, from the stage when young stars are completely obscured by their dusty gas cocoons to the stage of a young star cluster with no evidence of the ionized gas (Lada & Lada 2003). Whitmore et al. (2011) developed an evolutionary classification scheme of star clusters based on *Hubble Space Telescope* (HST) observations of M83. Star clusters become visible in optical bands since the age of ~ 2.5 Myr (Kim et al. 2021, 2023). The authors showed that in clusters with ages between 2 and 4 Myr, the ionized

* E-mail: gusev@sai.msu.ru

Table 1. The galaxy sample.

Galaxy	Type	B_r (mag)	$M(B)^d$ (mag)	i (deg)	PA (deg)	R_{25}^b (arcmin)	D (Mpc)	$A(B)_{\text{Gal}}$ (mag)	$A(B)_{\text{in}}$ (mag)	n	Data ^c
1	2	3	4	5	6	7	8	9	10	11	12
NGC 245	SA(rs)b	12.72	-21.12	21	145	0.62	53.8	0.097	0.04	33	Ph ¹
NGC 266	SB(rs)ab	12.27	-21.94	15	95	1.55	63.8	0.252	0.01	19	Ph ¹ + H α ²
NGC 628	SA(s)c	9.70	-20.72	7	25	5.23	7.2	0.254	0.04	497	Ph ³ + H α ⁴ + Sp ⁵⁻¹⁵
NGC 783	Sc	13.18	-22.01	43	57	0.71	70.5	0.222	0.45	32	Ph ^{16,17} + Sp ¹²
NGC 2336	SAB(r)bc	11.19	-22.14	55	175	2.51	32.2	0.120	0.41	48	Ph ¹⁸ + H α ¹⁹ + Sp ¹²
NGC 3184	SAB(rs)cd	10.31	-19.98	14	117	3.79	10.2	0.060	0.02	109	Ph ^{20,21} + H α ²¹ + Sp ^{5,8,13,22}
NGC 3726	SAB(r)c	10.31	-20.72	49	16	2.62	14.3	0.060	0.30	129	Ph ^{23,24} + H α ²⁵ + Sp ²²
NGC 4136	SAB(r)c	11.92	-18.38	22	30	1.20	8.0	0.066	0.05	11	Ph ²⁶ + Sp ²²
NGC 5351	SA(r)b	12.57	-21.16	60	101	1.20	51.1	0.074	0.40	16	Ph ^{24,27} + Sp ²²
NGC 5585	SAB(s)d	10.94	-18.73	53	34	2.13	5.7	0.057	0.38	69	Ph ²⁸ + H α ²⁹ + Sp ²²
NGC 5605	(R)SAB(rs)c	12.58	-20.86	36	65	0.81	44.8	0.318	0.15	6	Ph ³⁰
NGC 5665	SAB(rs)c	12.25	-20.42	53	151	0.95	31.1	0.091	0.35	7	Ph ³⁰
NGC 6217	(R)SB(rs)bc	11.89	-20.45	33	162	1.15	20.6	0.158	0.22	28	Ph ^{1,31} + H α ² + Sp ¹²
NGC 6946	SAB(rs)cd	9.75	-20.68	31	62	7.74	5.9	1.241	0.04	320	Ph ¹ + H α ³² + Sp ^{5-7,11,33,34}
NGC 7331	SA(s)b	10.20	-21.68	75	169	4.89	14.1	0.331	0.61	100	Ph ^{1,35} + H α ³² + Sp ^{9,12}
NGC 7678	SAB(rs)c	12.50	-21.55	44	21	1.04	47.8	0.178	0.23	22	Ph ^{1,36} + Sp ¹²
NGC 7721	SA(s)c	11.11	-21.18	81	16	1.51	26.3	0.121	0.98	36	Ph ¹
IC 1525	SBb	12.51	-21.89	48	27	0.97	69.6	0.410	0.24	15	Ph ³⁷
UGC 11973	SAB(s)bc	13.34	-22.47	81	39	1.73	58.8	0.748	0.85	13	Ph ¹ + Sp ³⁸

^a The absolute magnitude of a galaxy corrected for Galactic extinction and inclination effects.

^b The radius of a galaxy at the isophotal level 25 mag arcsec⁻² in the B band corrected for Galactic extinction and inclination effects.

^c References: 1 – Gusev et al. (2015), 2 – Epinat, Amram & Marcelin (2008), 3 – Bruevich et al. (2007), 4 – Gusev & Efremov (2013), 5 – McCall, Rybski & Shields (1985), 6 – Belley & Roy (1992), 7 – Ferguson, Gallagher & Wyse (1998), 8 – van Zee et al. (1998), 9 – Bresolin, Kennicutt & Garnett (1999), 10 – Rosales-Ortega et al. (2011), 11 – Cedrés et al. (2012), 12 – Gusev et al. (2012), 13 – Sánchez et al. (2012), 14 – Berg et al. (2013), 15 – Berg et al. (2015), 16 – Gusev (2006a), 17 – Gusev (2006b), 18 – Gusev & Park (2003), 19 – Young et al. (1996), 20 – Larsen & Richtler (1999), 21 – Gusev & Kaisin (2002), 22 – SDSS, 23 – Gusev et al. (2002), 24 – Gusev et al. (2018), 25 – Knapen et al. (2004), 26 – Gusev, Zasov & Kaisin (2003), 27 – Gusev & Kaisin (2004), 28 – Bruevich, Gusev & Guslyakova (2010), 29 – Dale et al. (2009), 30 – Artamonov, Badan & Gusev (2000), 31 – Artamonov et al. (1999), 32 – Gusev et al. (2016), 33 – García-Benito et al. (2010), 34 – Gusev, Sakhibov & Dodonov (2013), 35 – Regan & et (2004), 36 – Artamonov, Bruevich & Gusev (1997), 37 – Bruevich, Gusev & Guslyakova (2011), 38 – Gusev, Sakhibov & Ezhkova (2020).

gas is observed in the same place as the cluster stars. Clusters of ages $\approx 4-5$ Myr are surrounded with small H II bubbles whose radii are equal to 7–20 pc (Whitmore et al. 2011). The phase of the partially embedded cluster blowing a bubble of gas is rather short, it lasts for about 1–3 Myr (Hollyhead et al. 2015; Kim et al. 2021, 2023). Star clusters with ages of > 5 Myr are surrounded by a large ionized gas bubble. The radii of the bubbles are larger than 20 pc. The ionized gas is not detected around star clusters of ages > 10 Myr. Fig. 1 illustrates this evolutionary sequence on the sample of our young unresolved objects.

A study of the earliest stages of star clusters, OB associations and their complexes and estimation of physical parameters therein are difficult tasks because of the impact of gas and dust on the observations. Perhaps the most difficult task is to estimate ages of stellar populations. Usually, 2D or 3D spectroscopic or photometric data, or their combination are used for estimating ages of unresolved extragalactic star clusters. The spectroscopic method involves both estimation of spectral age indicators [e.g. equivalent widths $EW(H\alpha)$ and $EW(H\beta)$, $[O III]/H\beta$ ratio, He II emission lines, etc.] and a direct comparison of spectra with synthetic spectra of different ages (Copetti, Pastoriza & Dottori 1986; Bastian et al. 2005, 2006, 2009; Konstantopoulos et al. 2009; Wofford, Leitherer & Chandar 2011). The photometric method involves comparison of multicolour photometry data for clusters with predictions of evolutionary synthesis models (Searle, Wilkinson & Bagnuolo 1980; Elson & Fall 1985; Bresolin & Kennicutt 1996; Chandar et al.

2010; Hollyhead et al. 2015, 2016; Adamo et al. 2017; Turner et al. 2021).

Comparison shows that ages, evaluated for the same star clusters using data of spectral and photometric observations are in a fairly good agreement (see e.g. Searle et al. 1980; Whitmore et al. 2011; Wofford et al. 2011). However, Kim et al. (2012), who studied resolved stellar populations in star formation regions of M83 found that correlation between the ages of star clusters determined from individual stars in the region and the ages obtained via integrated colours using a standard photometric method is not very strong. This discrepancy, in addition to the reasons indicated by Kim et al. (2012) ($H\alpha$ emission impact, selection effects for stars, overlay of isochrones for 1 and 3 Myr), we tend to explain also by the use of a continuously populated initial mass function (IMF) and the presence of a small but significant range of ages of stars in the clusters.

Spectroscopic techniques usually provide age estimates (see e.g. García-Benito et al. 2010), however the method allows determination of ages for a limited number of objects. One of the main challenges in photometric age estimation is accounting for the effect of gas and dust on observations. A lack of independent data on the chemical abundance and extinction in the clusters leads to ‘age–extinction’ and ‘age–metallicity’ degeneracies in the comparative analysis with the theoretical evolutionary models of star clusters (Scalo 1986). Moreover, continuum and line emissions from the ionized gas are strong enough to affect the integrated broad-band photometry (Reines et al. 2010).

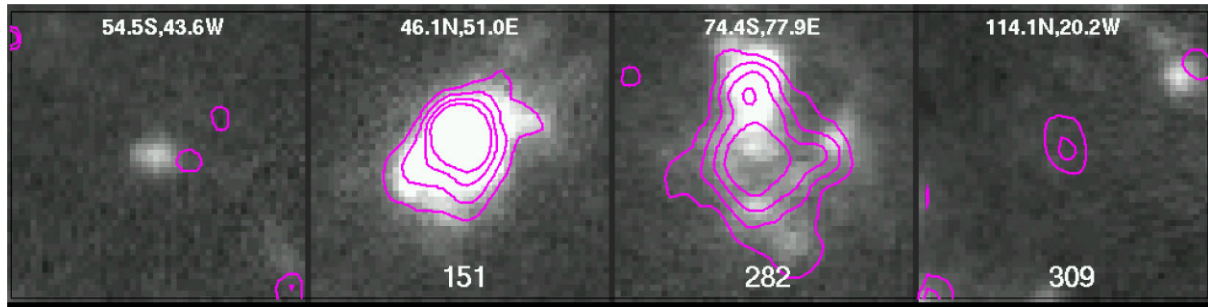


Figure 1. $H\alpha$ images of star formation regions in NGC 628 with superimposed isophotes 22.0, 21.5, 21.0, and 20.5 mag arcsec $^{-2}$ in the U band are shown. Galactocentric coordinates of centres of the images (top) and serial numbers from the catalogue, if any, (bottom) are given. The size of the images is 13.6×13.6 arcsec 2 . North is upwards and east is to the left. See the text for details.

Age and mass estimates based on long-slit spectroscopic observations are correct only if the radiation of stars, which form the continuum of the spectrum, spatially coincides with the ionized gas emission. This situation is observed in star formation regions younger than ≈ 5 Myr (Whitmore et al. 2010). The combination of optical photometric, $H\alpha$ spectrophotometric and spectroscopic observations provides us with the necessary data to separate spatially the radiation from gas and stellar components. This makes it possible to take into account the contribution of the gas to the optical photometric bands and to find objects in which the light extinction for the stars is equal to the light extinction for the emission of ionized gas (Gusev et al. 2016, 2018).

Note that for stellar clusters [simple stellar population (SSP) systems] with masses less than $5 \times 10^3 - 10^4 M_{\odot}$, stochastic effects in the discrete random population IMF start playing a key role and applying the ‘standard’ mode of continuous IMF models will not be correct (Whitmore et al. 2010; Piskunov et al. 2011). According to Cervino (2013), IMF discreteness significantly affects the luminosity and colour of the cluster. The strength of this effect depends on the wavelength and is particularly strong in IR wavelengths, where the effect of discreteness is noticeable up to $M_{cl} \sim 10^7 M_{\odot}$ masses, rather than $10^4 M_{\odot}$ as at optical wavelengths in the V band. Thus, the estimation of physical parameters of stellar groupings, using photometric methods with a continuously populated IMF is correct only for massive star clusters.

This paper presents the conclusive part of our project of comprehensive study of star formation regions in the selected 19 spiral galaxies. The results of our own spectroscopic observations of 103 H II regions in 8 galaxies were presented in the previous papers (Gusev et al. 2012, 2013, 2020). In Gusev et al. (2016), we estimated physical parameters of stellar population in H II regions using a combination of spectroscopic (Gusev et al. 2012, 2013) and photometric observations (see Table 1). We derived properties of extracted emission spectra of H II regions and estimated their extinctions, chemical abundances, and the relative contributions of nebular continuum and emission lines to the total observed flux. These data were used to obtain the luminosities and colour indices of stellar groupings, corrected for extinction and nebular emission contribution, i.e. ‘true’ (intrinsic) colours and luminosities of stellar population. As a result, we were able to estimate ages and masses for ≈ 60 per cent of clusters (complexes) of our sample. Extinctions for ≈ 35 per cent of objects were overestimated. This is due to the fact that the key assumption of our method, the equality of the light extinction for stars, $A(\text{stars})$, and the light extinction for ionized gas, $A(\text{gas})$, is not satisfied for a significant number of young clusters.

The fact that the extinction in a gaseous medium is up to two times higher than the stellar one is a well-known fact for a long time (Calzetti 2001). Sakhibov & Smirnov (1995) empirically investigated the discrepancy between the extinction of gas emission and the extinction of stellar light in the giant H II regions, i.e. in star formation complexes in galaxies M33, LMC, and NGC 2403. They found that, in most cases, $A(\text{Balmer}) \equiv A(\text{gas})$ is higher than $A(\text{stars})$. Such a result can be explained in terms of the quite uneven distribution of obscuring material (Caplan & Deharveng 1986). So, using correction of the observed colours of stars in the star formation complexes for extinction in the Balmer lines can result in a bias in the colours of the stars in the complexes towards the blue part of the spectrum, thus distorting the parameters of star formation derived from these colours. Objects with $A(\text{gas}) \neq A(\text{stars})$ have a high nebular emission contribution in the U , B , and V bands (> 40 per cent) and an extremely high $\text{EW}(H\alpha) > 1500 \text{ \AA}$. Visually, in these regions a spatial displacement between the photometric centres of the stars in the broad-bands and of the gas emissions in $H\alpha$ line is observed (see the third image from left in Fig. 1).

Later, we presented the catalogue of 1510 young stellar groupings associated with H II regions in 19 galaxies in Gusev et al. (2018) using multicolour photometric and $H\alpha$ ($H\alpha + [\text{N II}]$) spectrophotometric observations. This catalogue is available in electronic form.¹ In the same paper, we modified our extinction and age estimation techniques using $H\alpha$ morphology as an additional indicator. This method was developed in Whitmore et al. (2011).

The goal of this study is to estimate the physical parameters, such as mass and age, of the stellar population in the star formation regions of the galaxies of our sample, using additional spectral data for H II regions taken from the literature and open data bases.

Most of the stellar groupings studied in this paper have an age of $\sim 1-10$ Myr, i.e. they are objects with $H\alpha$ emission, visible at optical wavelengths. In addition, we studied young star clusters with colour indices typical for stellar populations younger than 10 Myr without visible $H\alpha$ emission including the cases for which $H\alpha$ data are absent for the galaxy. These young objects may be older than 10 Myr (see Section 3.2 for details).

The sample of selected galaxies is based on our $UBVRI$ photometric survey of 26 galaxies (Gusev et al. 2015). Numerous star formation regions are observed visually in 19 of them. The sample is presented in Table 1, where data on the Galactic extinction, $A(B)_{\text{Gal}}$, are taken from the NED² data base, and the other parameters are taken

¹http://lnfm1.sai.msu.ru/~gusev/sfr_cat.html

²<http://ned.ipac.caltech.edu/>

from the LEDA³ data base (Paturel et al. 2003). The morphological type of the galaxy is listed in column (2). The apparent and absolute B magnitudes are presented in columns (3) and (4). The inclination and position angles are given in columns (5) and (6). The isophotal radii in units of arcmin are shown in column (7). The adopted distances are given in column (8). The Galactic extinction and the dust extinction due to the inclination of a galaxy are listed in columns (9) and (10). The number of identified star formation regions in the galaxy is shown in column (11). A presence of photometric (Ph) and $H\alpha$ spectrophotometric observations of the galaxies, as well as spectrophotometric and spectroscopic (Sp) data for the star formation regions and the references to them are given in column (12). The adopted value of the Hubble constant in the study is equal to $H_0 = 75 \text{ km s}^{-1} \text{ Mpc}^{-1}$.

2 DATA AND METHODS USED

The algorithm and techniques for data reduction, criteria for selecting star formations regions, and evolutionary synthesis models used were described in detail in our previous paper (Gusev et al. 2013, 2016, 2018; Gusev & Shimanovskaya 2019). In this paper, we describe only the new data and models used, as well as the data considered earlier very briefly.

2.1 Observational data

Most part of our own observations was published earlier (see Table 1). Additionally, we used FITS images of the galaxies which were taken from the NED data base, as well as spectroscopic data from the Sloan Digital Sky Survey (SDSS) DR13⁴ (Albareti et al. 2017) and from the literature (see references in Table 1).

2.1.1 Photometric and spectrophotometric $H\alpha$ images

Earlier we carried out photometric observations of 19 galaxies, studied here, and published the analysis of the photometric data (see Gusev et al. 2015, 2018, and references therein, see also notes in Table 1).

Spectrophotometric $H\alpha$ observations of NGC 3184 and $H\alpha + [\text{N II}]$ observations of NGC 628, NGC 6946, and NGC 7331 were described in our previous papers (Gusev & Kaisin 2002; Gusev & Efremov 2013; Gusev et al. 2016). FITS images, obtained with narrow-band interference $H\alpha + [\text{N II}]$ or $H\alpha$ filters for another five galaxies from our sample, were found in the NED data base (see references in Table 1).

We used the $H\alpha + [\text{N II}]$ FITS image of NGC 3726 obtained by Knapen et al. (2004). Parameters for absolute calibration of $H\alpha + [\text{N II}]$ flux to units of $\text{erg s}^{-1} \text{ cm}^{-2}$ were found in descriptors of the FITS file. Absolute calibration of the FITS image of NGC 5585 from Dale et al. (2009) was done according to the data in descriptors of the FITS file. Additionally, we checked the calibration using integrated $H\alpha + [\text{N II}]$ fluxes of NGC 5585 measured in James et al. (2004) and Kennicutt et al. (2008). For a study of H II parameters in NGC 2336, we used the $H\alpha + [\text{N II}]$ FITS image obtained in Young et al. (1996). FITS file descriptors and results of integrated $H\alpha + [\text{N II}]$ photometry from Young et al. (1996) were used for absolute flux calibration. For two galaxies (NGC 266 and NGC 6217), we used $H\alpha$ FITS images published in Epinat et al.

(2008). Their absolute calibrations were carried out using the results of integrated $H\alpha$ photometry of Epinat et al. (2008) for NGC 266 and NGC 6217, and integrated spectrophotometry of James et al. (2004) for NGC 6217. Note that the absolute calibration uncertainty of NGC 266 and NGC 6217 can reach $\approx 20\text{--}25$ per cent. This accuracy, however, is sufficient for estimates of nebular emission contributions in total fluxes from star formation regions in galaxies (Gusev et al. 2016, 2018).

2.1.2 Spectroscopic data for star formation regions

The results of spectroscopic observations of 103 H II regions in eight galaxies have already been published in our previous papers (Gusev et al. 2012, 2013, 2020). An explicit description of the observational data reduction is given in Gusev et al. (2012). Additionally, in this paper we used data of emission line spectrophotometry, integral field spectroscopy, and long-slit spectroscopy for H II regions in the galaxies in our sample from the literature and SDSS (see notes in Table 1).

Among 19 galaxies of our sample, we found spectral data for H II regions in NGC 628, NGC 3184, NGC 6946, and NGC 7331 in the literature. Some H II regions in NGC 3184, NGC 3726, NGC 4136, NGC 5351, and NGC 5585 were observed in the SDSS project.

At the first stage, we cross-identified the H II regions observed by different authors. Then these regions were identified with the objects from our catalogue (see Sections 2.2 and 3.1).

A description of calculation of the extinction coefficient, $c(H\beta)$, from the measured Balmer decrement was presented in Gusev et al. (2012).

Oxygen abundances, O/H, in H II regions were obtained using the reddening-corrected fluxes in the main emission lines $[\text{O II}] \lambda 3727 + 3729$, $[\text{O III}] \lambda 4959 + 5007$, $[\text{N II}] \lambda 6548 + 6584$, and $[\text{S II}] \lambda 6717 + 6731$. Because different sets of emission lines were measured in different studies, we used four different empirical calibration methods. In order of priority, these are S calibration (Pilyugin & Grebel 2016), R calibration (Pilyugin & Grebel 2016), O3N2 calibration (Pettini & Pagel 2004; Marino et al. 2013), and H II-ChiMistry method (Pérez-Montero 2014). We also took our O/H data from Gusev et al. (2012) measured using NS calibration (Pilyugin & Mattsson 2011).

For objects, observed in several studies, we took weighted averages of the measured abundances, extinctions, and $H\alpha$ equivalent widths with weights inversely proportional to their relative measurement uncertainties.

We used all available data (our, SDSS, and from the literature) to find the mean values, with one exception. Spectrophotometric measurements of Belley & Roy (1992) for NGC 628 and NGC 6946 were used only for objects which were not observed by any other authors. This is because the spectrophotometry results of Belley & Roy (1992) are not as accurate as spectroscopic ones for individual objects (see Bruevich et al. 2007, for details). We also do not include recently published measurements made for H II regions in NGC 628 within inner 1.5 effective radii based on integral field unit (IFU) spectroscopy with MUSE/VLT (Groves et al. 2023), but compare the results in Section 3.2.

2.2 Sample selection

The procedure of selection of young stellar groupings was described in detail in Gusev et al. (2018). We note briefly that the preliminary

³<http://leda.univ-lyon1.fr/>

⁴<http://www.sdss.org/dr13/>

selection of bright star formation sources from B and $H\alpha$ images of galaxies was carried out with the use of the SEXTRACTOR⁵ programme. We searched stellar groupings associated with H II regions and young star clusters with colour indices corresponding to stellar populations younger than 10 Myr.

The final selection criteria for the objects, included in our catalogue, have been explained in Gusev et al. (2018). The selected young stellar groupings must satisfy one of the following conditions: (i) those, which form close pairs with the nearest H II regions: the angular separation between photometric centres of the stars in B band and the gas emission in $H\alpha$ is less than 1.5 arcsec (in 9 galaxies with obtained $H\alpha + [N II]$ or $H\alpha$ images), (ii) those, for which the emission spectra are measured (in 13 galaxies with obtained spectroscopic data), (iii) those, which have corrected for the Galactic extinction and inclination effects $(U - B)_0^i < -0.537$ mag (in 16 galaxies for which U images have been obtained), and (iv) those, which have $(B - V)_0^i < -0.043$ mag (in NGC 4136, NGC 5605, NGC 5665, and outer part of NGC 7331).

Remark that the ambiguity of age from $U - B$ and $B - V$ values exists for stellar systems with ages between 6 and 40 Myr. Stellar groupings with $(U - B)_0^i$ colour indexes ranging from -0.75 to -0.5 can be both older and younger than 10 Myr (Gusev et al. 2018).

2.3 Young stellar groupings and gas-to-stars morphology

As we noted in Gusev et al. (2016), the technique, that we use to determine the age and mass of the stellar component of star formation regions, has some limitations. The spatial displacement between photometric centres of stars and of gas emissions in star formation regions leads to incorrectly estimated extinction and overestimated contribution of nebular emission in optical broad-bands. Physical parameters (age and mass) of stellar population in star formation regions can be correctly retrieved only provided that the optical radiation from stars spatially coincides with ionized gas emission. A typical sample of such regions is shown on the second image from left in Fig. 1.

If both optical broad-band and $H\alpha$ images of a galaxy are available, it is possible to detect a presence or an absence of the spatial displacement by direct comparison of the positions of photometric centres in these bands. For galaxies, that were not observed in $H\alpha$ line, we can suspect the displacement by spectral features, such as an extremely large $EW(H\alpha)$ ($> 1500\text{\AA}$), an extremely high nebular emission contribution (> 40 per cent) in the shortwave optical bands, an extremely large Balmer decrement, giving unrealistically ‘blue’ colour indices (Gusev et al. 2016).

For objects with a star-like profile, we accept that the photometric emission centres of stars and gas coincide if the distance between them in a plane does not exceed 0.5 arcsec (see Gusev et al. 2018, for details).

In addition to the objects where the optical emission from stars coincides with the $H\alpha$ emission from ionized gas, we can obtain physical parameters of young star clusters without a visible $H\alpha$ emission. These star clusters have the extinction that is close to zero (Whitmore et al. 2011), thus we can assume $A(\text{stars}) = A_{\text{Gal}} + A_{\text{in}}$, where A_{Gal} is the Galactic extinction and A_{in} is the dust extinction due to the inclination of a galaxy [see columns (9) and (10) in Table 1]. A sample of such regions is shown on the right image in Fig. 1.

We have classified the young stellar groupings studied here as follows:

class 2 – optical radiation from stars coincides with ionized gas emission (second image from left in Fig. 1);

class 1 – photometric (stellar) radiation centre is displaced from gas emission centre (third image from left in Fig. 1);

class 0 – no gas emission within the area of optical radiation from stars (fourth image from left in Fig. 1);

class –1 – no $H\alpha$ data.

2.4 Comparison with synthetic models

We described in detail the algorithm for correction of observational photometric fluxes for contribution from nebular continuum and emission lines in Gusev et al. (2016). To briefly summarize: we determined the relative contributions of the stellar and nebular continua, and gas emission lines to the total observed flux in the $UBVRI$ bands following Sakhibov & Smirnov (1990).

We used the emission line ratios for every star formation region in our sample (see Section 2.1.2) to derive electron temperatures and metallicities in the H II regions. The fluxes for the non-measured emission lines were calculated based on the derived estimations of the emission measures, using the equations given in Kaplan & Pikelner (1979) and Osterbrock (1989). A total of 18 main emission lines were taken into account. The contribution from the gas line emission was computed through the summation of the emission line intensities in a given photometric band.

The relative contribution of the nebular continuum was estimated using the equations for the continuum emission near the limits of the hydrogen series emission, two-photon and free–free emissions, given in Lang (1978), Kaplan & Pikelner (1979), Brown & Mathews (1970), and Osterbrock (1989).

We used spectrophotometric $H\alpha$ ($H\alpha + [N II]$) fluxes (see Section 3.1) for the absolute calibration of the emission line spectroscopic fluxes. For two galaxies without $H\alpha$ photometry, NGC 4136 and NGC 5351, we multiplied the absolute fluxes, obtained within the SDSS aperture, by a factor, calculated as the ratio of the flux in the R band within the aperture that we used for every H II region to the flux within the area of the SDSS aperture. The reliability of this procedure was discussed in Gusev et al. (2016).

Obtained ‘true’ photometric parameters of the star groups, i.e. colours and magnitudes corrected for the extinction and gas contribution, were compared with SSP evolutionary sequences using Salpeter IMF with a mass range from 0.15 to $100 M_{\odot}$.

We used a data base of stellar evolutionary tracks and isochrones provided by the Padova group (Bertelli et al. 1994; Girardi et al. 2000; Marigo & Girardi 2007; Marigo et al. 2008) via the online server CMD.⁶ We used the sets of stellar evolutionary tracks from version 2.8 (Bressan et al. 2012; Tang et al. 2014; Chen et al. 2014, 2015).

For young massive clusters with $M > 1 \times 10^4 M_{\odot}$, models in *Standard* modes have been developed adopting the technique described in Piskunov et al. (2011). The standard mode reproduces properties of standard SSP models with a continuously populated

⁵<http://sextractor.sourceforge.net/>

⁶<http://stev.oapd.inaf.it/cgi-bin/cmd/>

IMF, while the extended mode allows to take into account the influence of a randomly populated IMF.

As we discussed earlier in Gusev, Egorov & Sakhibov (2014), the multiple structure of unresolved star complexes does not affect their integrated colour indices and therefore the estimations of the age of a stellar population.

Multicolour photometry provides a useful tool for constraining masses and ages of stellar populations in star formation regions. Here, we use the method of the minimization of ‘observed minus computed’ ($O - C$) parameters

$$O - C = [[(U - B)_{\text{obs}} - (U - B)_{\text{model}}]^2 + [(B - V)_{\text{obs}} - (B - V)_{\text{model}}]^2 + [M(B)_{\text{obs}} - M(B)_{\text{model}}]^2]^{1/2}, \quad (1)$$

described in Gusev et al. (2007, 2016), where under the concept of ‘observed parameters’ we place the ‘true’ colours $U - B$ and $B - V$, and B luminosities. We did not use the $V - R$ and $V - I$ colour indices because, in the case of star formation regions, the R and I fluxes are weakly sensitive to changes in age, and actual observational errors lead to large uncertainties. Moreover, the stochastic effects of the stellar luminosity function are noticeable up to $M_{\text{cl}} \sim 10^7 M_{\odot}$ masses, rather than $10^4 M_{\odot}$ as at optical wavelengths in U , B , and V bands (Cerviño 2013). The exception is a few objects without gas emission within the area of optical radiation from stars, for which observations in the U band are unavailable. For them, we used the ‘true’ colours $B - V$ and $V - R$.

The stellar population models, computed for Z , independently obtained from observations, are presented in the form of a grid of models for a broad range of variation of parameters $t(i)$ and $M(j)$, where the indices i, j are the numbers of rows and columns in a two-dimensional grid of physical parameters. The table step h of the $\log t$ parameter variation is 0.05 dex. The initial table step of the $\log M$ for the first iteration depends on the range of luminosity variations of star formation regions in a given galaxy:

$$h_{\log M} = (\log M_{\text{max}} - \log M_{\text{min}})/N,$$

where N is the number of the evolutionary sequences simulated for N values of cluster masses within a given mass interval. For every node (i, j) , the value of the $(O - C)_{i,j}$ parameter was calculated. The second step is the search for the grid node in which the $(O - C)_{i,j}$ parameter has a minimum value.

Note that the value of the parameter $(O - C)_{i,j}$ corresponds to the distance of the investigated stellar cluster from the grid node (i, j) in the three-dimensional photometric space of $U - B$, $B - V$, and M_B . The minimum value of $(O - C)_{i,j}$ corresponds to the distance between the object under study and the nearest node in the photometric value space. This lowest parameter value $(O - C)_{i,j}^{\text{min}}$ had to be less than the errors of the observed colours and luminosities. Otherwise, the next iteration was carried out, in which the mass interval was halved and centred according to the results of the previous iteration. Thus, beginning with the second iteration, for each stellar grouping under study, a particular grid of models was simulated according to the input observational data $[M(B)_{\text{obs}}, (U - B)_{\text{obs}}, (B - V)_{\text{obs}}, Z]$. With each successive iteration, the density of the model grid was increased. The number of iterations per object needed to achieve the requirement $(O - C)_{i,j}^{\text{min}}$ less than the observational error of photometric quantities, Δ_{U-B} , Δ_{B-V} , Δ_{M_B} , ranged from 2 to 4. The values of age $t(i)$ and mass $M(j)$ corresponding to the selected node (i, j) with the minimum value of parameter $(O - C)_{i,j}^{\text{min}}$, were taken as the age t_{cl} and mass M_{cl} for the stellar grouping under study. Simultaneous constraint using equation (1) and true colours

and luminosities in the U , B , and V bands, which are most sensitive to changes of age and mass, with a grid of models simulated for metallicity, which is fixed from independent observations, helps to avoid ambiguities associated with degenerations of ‘metallicity–age’, ‘absorption–age’, ‘luminosity–mass’ and ambiguity in the estimates of physical properties, age t_{cl} and mass M_{cl} , within the adopted model.

The model grid of *Extended* mode was constructed using Monte Carlo simulations by which random variations of the discrete IMF depending on a given model star cluster mass were generated. For every given cluster mass, a discrete IMF was generated using a pseudo-random number generator. Note that with this random sampling of the discretely populated IMF for a fixed mass value of the stellar grouping, the number of stars, N_{stars} in that grouping is also fixed. Then, using this randomly chosen discrete IMF, we have calculated an evolutionary sequence of 68 models of *Extended* mode for every given cluster mass with a $\log t$ -step of 0.05 in the interval $\log t = 5.9 - 9.3$ and metallicity Z fixed from the observations. For each calculation of a randomly sampled discrete IMF, a random seed was used, also obtained using a pseudo-random number generator. When comparing the observed colours and luminosity of a given object with that of a model, each iteration uses $N = 50$ evolutionary sequences of ‘discrete’ models of *Extended* mode. The number of iterations per object ranged from 2 to 4. So the number of simulations of a randomly sampled discrete IMF per object varies from 50 to 200. Number of simulated *Extended* mode models for each pair of mass M_{cl} and age t_{cl} estimates ranged from 6800 to 13 600.

The errors of the age and mass estimates for the case of continuous IMF models have been calculated as follows. Using the evolutionary sequences for the star cluster colour indices in the U , B , and V bands, simulated for a fixed model grid node (i, j) , the coefficients of the third- or fourth-degree interpolation polynomial were calculated for a time interval corresponding to the selected node (i, j) with a minimum value of the parameter $(O - C)_{i,j}$. Knowing the functional (polynomial) correlation between colour and age, and the observational error of the colours used, we applied the Gauss law of error propagation to determine the accuracy of the age estimates. Similarly, using the functional correlation between the model luminosity and the cluster mass, as well as the observational errors of the integrated luminosities, the accuracies of the mass estimates were defined.

The IMF discreteness significantly affects the luminosity and colours of the cluster, as manifested by flashes and fluctuations in the evolutionary path of the cluster’s photometric parameters, caused by the appearance of red giants. There is also a systematic bias between luminosities and colours of main-sequence clusters and the predictions by standard SSP models (see Fig. 2 and more details in Piskunov et al. 2011). The luminosity evolution curve of the discrete cluster model has the form of tilted oscillations and consists of relatively short time-scale intervals of recurrent events. During a single time interval, there are a slow, gradual increase in cluster luminosity and an almost instantaneous outburst, caused by the evolution of the brightest star in the main sequence and its eventual transformation into a bright, short-lived red supergiant. After the supergiant’s decline, the process is repeated by the evolution of the next brightest star on the main sequence and its transformation into a red giant. Note that the behaviour of the colour and luminosity evolution curves of the discrete model, described above, is stronger in the case of small cluster masses M_{cl} , when the number of red giants is rare and the clusters spend most of the time as clusters with stars of the main sequence. As the cluster mass M_{cl} increases, the colour and luminosity evolution curves of the discrete model converge to those of the standard continuous model.

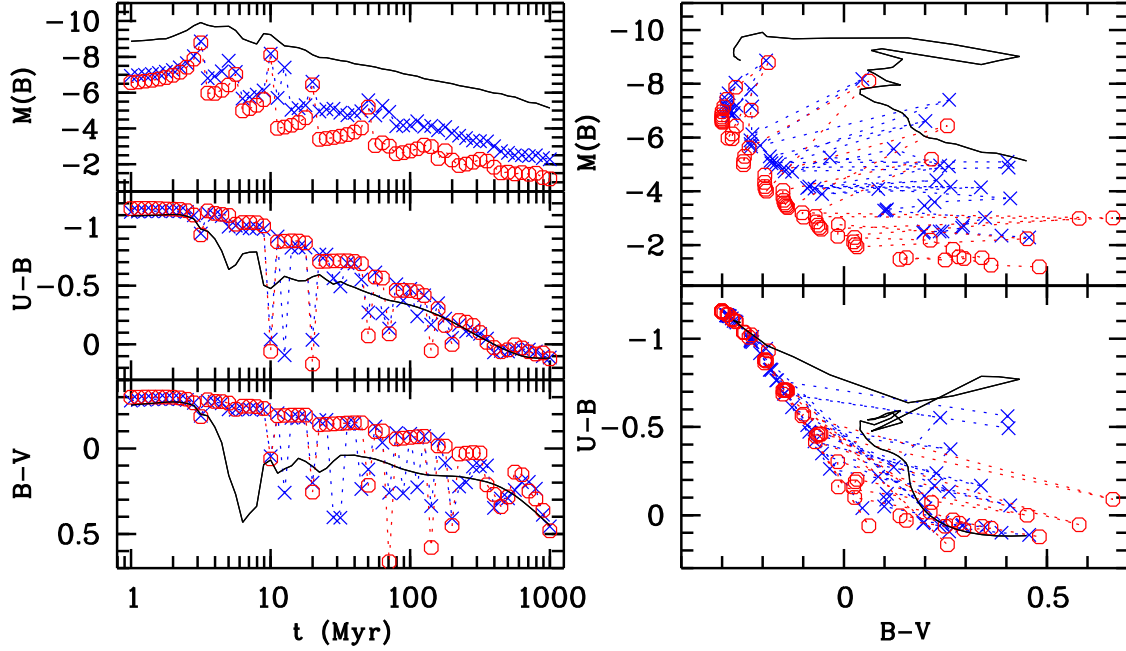


Figure 2. Samples of evolutionary sequences of the *Standard SSP mode* (continuously populated IMF) for a stellar system with $Z=0.012$ and $M = 1 \times 10^4 M_{\odot}$ (black curves), and the *Extended SSP mode* (randomly populated IMF) for stellar systems with $Z = 0.012$ and $M = 1 \times 10^3 M_{\odot}$ (blue crosses connected by dotted lines) and $M = 500 M_{\odot}$ (red circles connected by dotted lines). Variations of absolute magnitude $M(B)$ and colour indices $U - B$ and $B - V$ versus age (left) and colour–magnitude and colour–colour diagrams (right) for the synthetic evolutionary sequences are shown. See the text for details.

The errors of the age and mass estimates for the case of discrete IMF models have been calculated as follows. Based on the model colours corresponding to the selected node (i, j) with the minimum value of parameter $(O - C)_{i,j}^{\min}$, the corresponding interval on the colour evolution curve of the discrete model between two ‘red flashes’ was selected and the coefficients of the interpolation polynomial were calculated. Then, as in the case of the continuous model, knowing the functional relationship between age and colour, as well as colour observation errors, we applied the Gauss law of error propagation to determine the accuracy of the age estimates. Similarly, using the functional correlation between the model luminosity and the cluster mass within the interval between two ‘red flashes’, as well as observational errors of the integrated luminosities, the accuracies of the mass estimates were determined.

In summary, the errors of age and mass estimates, calculated here, take into account the influence of colour and luminosity observation errors only. The influence of the accuracy of the choice of a model grid node, on the estimates of ages and masses, we have not considered, just making sure that the minimum parameter $(O - C)_{i,j}^{\min}$ must not exceed the observational error of the colours and luminosities, $\Delta_{U-B}, \Delta_{B-V}, \Delta_{M_B}$. We have therefore not detected the effect of increasing inaccuracy when considering discrete models of small masses.

We compared the mass and age estimates, obtained using the continuously and randomly populated IMF, in Fig. 3. The top diagrams show that M_{rand} and t_{rand} are systematically larger than M_{cont} and t_{cont} , respectively. This difference decreases for high massive ($M > 5 \times 10^4 M_{\odot}$) and ageing ($t > 50$ Myr) stellar groupings. The differences between the mass estimates, obtained from continuous and random models for groups in the mass range of $5 \times 10^3 - 10^4 M_{\odot}$, are larger than for groups of higher mass. Above we have already noted the effect of IMF discreteness on the luminosity of the cluster, which is manifested by a systematic bias between luminosities

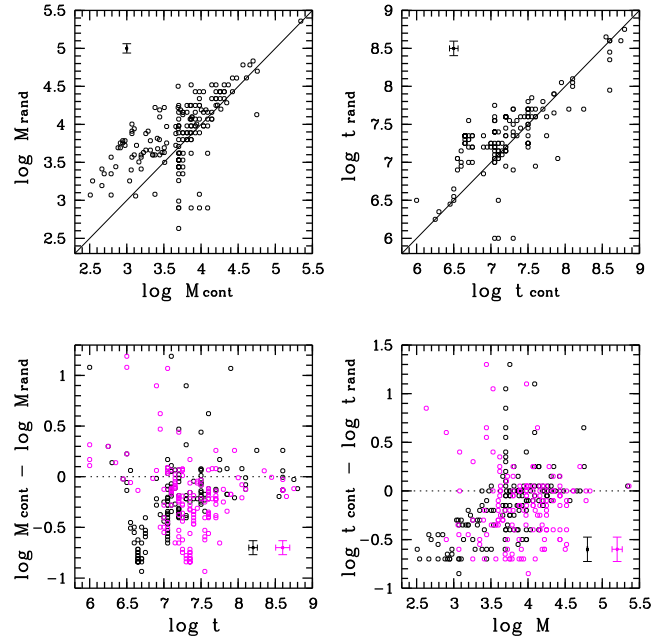


Figure 3. Comparison between masses (top-left panel) and ages (top-right panel) retrieved using evolutionary sequences with continuously and randomly populated IMF. One-to-one lines are shown. Dependencies ‘difference between masses estimated using continuously and randomly populated IMF, $\log M_{\text{cont}} - \log M_{\text{rand}}$, over age, $\log t'$ (bottom-left panel), and ‘difference between ages estimated using continuously and randomly populated IMF, $\log t_{\text{cont}} - \log t_{\text{rand}}$, over mass, $\log M'$ (bottom-right panel). Objects with ages (masses), estimated using continuously populated IMF, are shown by black circles, and ones with ages (masses), estimated using randomly populated IMF, are indicated by magenta circles in the bottom panels. Mean error bars are given.

of main-sequence clusters with randomly populated IMF and the predictions by standard SSP models noted in Bruzual (2002) and discussed thoroughly in Piskunov et al. (2011) and Cerviño (2013). The strength of this bias between the luminosities of the discrete and standard models is stronger at low masses and decreases with increasing cluster mass, which is apparent in our estimates of the masses of the stellar groupings explored here.

The maximum differences in age estimates are observed for objects with $t = 5\text{--}12$ Myr (Fig. 3). This difference results from the fact that in this age interval, the number of red giants in the case of the randomly populated IMF is rare and most of the cluster stars are main-sequence stars. Models with a continuously populated IMF and ages $t = 5\text{--}12$ Myr always contain red giants, which shift their colours towards red relative to those of models with a discrete IMF. With increasing age, the colour bias between continuous and discrete IMF models decreases. The bias also decreases at low ages $t < 5$ Myr (see fig. 7 in Piskunov et al. 2011). The use of various methods for determining ages in the range of 5–10 Myr gives results that differ by an order of magnitude or more (see e.g. Kim et al. 2012; Popescu, Hanson & Elmegreen 2012; Messa et al. 2018).

The maximum difference in $\log M_{\text{cont}} - \log M_{\text{rand}}$ is observed for objects with $t_{\text{cont}} = 5\text{--}12$ Myr and $t_{\text{rand}} = 10\text{--}30$ Myr (Fig. 3). For the youngest ($t < 4$ Myr) and oldest ($t > 50$ Myr) stellar groupings, it usually does not exceed 0.2 dex. The age difference $\log t_{\text{cont}} - \log t_{\text{rand}}$ is systematically negative for low massive objects with $M < 3 \times 10^3 M_{\odot}$. For most stellar groupings with $M > 5 \times 10^3 M_{\odot}$, this difference does not exceed 0.2 dex (Fig. 3).

In general, the data obtained in Fig. 3 correspond to the conclusions of Whitmore et al. (2010) and Piskunov et al. (2011) about the need to use models with a randomly populated IMF for star clusters with $M < 1 \times 10^4 M_{\odot}$, where the IMF discreteness effect is particularly strong. At low masses, models with a discrete IMF remain relatively long time like a main-sequence cluster model, free of red giants, due to their small number. Continuous models cannot resemble main-sequence clusters because they always contain a fraction of red giants. Therefore, at small masses, the luminosity of a branch of the main-sequence cluster can be 2–3 mag below the luminosity of a continuous track and colours are correspondingly bluer, $\Delta(B - V) \approx 0.1 - 0.5$ mag (Piskunov et al. 2011).

As noted by Cerviño (2013), the mean value of model simulations with a randomly sampled discrete populated IMF converges to the results of a ‘standard’ model with a continuously populated IMF. It is noted, however, that the ‘random sampling’ mode gives the entire distribution of possible age and mass values compared to the ‘standard mode’ for a set of photometric parameters fixed from the observations. At larger masses, on the other hand, the associated distributions approach Gaussians and the relative variance decreases (see Cerviño 2013, and references therein), so only the mean (and variance) is required for inference. Indeed, as the star cluster mass increases, the IMF population density increases, converging to a continuously populated IMF density and the results converge to the inferences of the ‘standard’ model. Thus, when at $M_{\text{cl}} \geq 10^4 M_{\odot}$ the bias between the discrete and continuous models is comparable or less than the errors of our observations and the application of continuously populated IMF models is more rational to reduce computational time.

In closing Section 2, we note again, that the bias between the discrete and continuous models is consistent with the above noted systematic excess of M_{rand} over M_{cont} , especially at low masses, where the number of red flashes in the case of a discrete IMF is rare and the luminosity of the cluster is determined by the emission of main-sequence stars. Since the continuous IMF models have for a

given mass a luminosity excess compared to discrete mass models, the former option requires lower luminosity in order to agree both models. Older age estimates, obtained with the discrete model, can be similarly explained by the blue colour bias of the discrete models with respect to continuous option.

3 RESULTS

3.1 Catalogue of young stellar groupings

The catalogue is available in electronic form at http://lnfm1.sai.msu.ru/~gusev/sfr_cat.html and is also presented as the additional online material on the paper page of the MNRAS website.

The following data are presented in the catalogue columns:

- (1) ID of the region;
- (2) galaxy name (NGC, IC, or UGC);
- (3) ID of the object within a galaxy;
- (4, 5) apparent coordinates in the plane of the sky, with respect to the galaxy centre, in units of arcseconds; positive values correspond to the northern (4) and western (5) positions;
- (6, 7) deprojected galactocentric distances in units of kpc (6) and in units of isophotal radius R_{25} (7), where R_{25} is the radius at the isophotal level 25 mag arcsec⁻² in the B band corrected for the Galactic extinction and inclination effects;
- (8) apparent total B magnitude;
- (9) absolute magnitude $M(B)$, $M(B) = B - 5 \log D - 25$, where D is an adopted distance in units of Mpc (see Table 1);
- (10) B magnitude uncertainty;
- (11–18) apparent colour indices $U - B$ (11), $B - V$ (13), $V - R$ (15), and $V - I$ (17) with their uncertainties (12, 14, 16, 18);
- (19, 20) logarithm of spectrophotometric $H\alpha + [\text{N II}]$ flux (19), where the flux is in units of erg s⁻¹cm⁻², for all galaxies except NGC 266, NGC 3184, and NGC 6217, and logarithm of $H\alpha$ flux for NGC 266, NGC 3184, and NGC 6217, and their uncertainties (20);
- (21) absolute magnitude $M(B)_0^i$, corrected for the Galactic extinction and inclination effects;
- (22–25) the colour indices ($U - B)_0^i$ (22), $(B - V)_0^i$ (23), $(V - R)_0^i$ (24), and $(V - I)_0^i$ (25), corrected for the Galactic extinction and inclination effects;
- (26) the same as column (19), but corrected for the Galactic extinction and inclination effects, $F(H\alpha + [\text{N II}])_0^i$ ($F(H\alpha)_0^i$);
- (27) $R - H\alpha$ index, $R - H\alpha = R + 2.5 \log F(H\alpha + [\text{N II}])$ for all galaxies except NGC 266, NGC 3184, and NGC 6217, and $R - H\alpha = R + 2.5 \log 1.35 F(H\alpha)$ for NGC 266, NGC 3184, and NGC 6217, where R is in magnitudes, and $F(H\alpha + [\text{N II}])$, $F(H\alpha)$ are the fluxes in units of erg s⁻¹cm⁻²;
- (28) gas-to-stars morphology [2 – optical radiation from stars coincides with ionized gas emission (class 2), 1 – photometric (stellar) radiation centre is displaced from the centre of gas emission (class 1), 0 – no gas emission within the area of optical radiation from stars (class 0), -1 – no $H\alpha$ data];
- (29, 30) extinction $A(B)$ and its uncertainty $\Delta A(B)$ in units of magnitude calculated from Balmer decrement;
- (31, 32) equivalent width $\text{EW}(H\alpha)$ in units of Å and its uncertainty;
- (33, 34) logarithm of equivalent width $\text{EW}(H\alpha)$ and its uncertainty;
- (35, 36) metallicity Z and its uncertainty;
- (37) relative contribution of nebular continuum and emission lines to the total observed flux in B band, $I_B(\text{gas})/I_B(\text{total})$;
- (38, 39) ‘true’ absolute magnitude $M(B)_{\text{true}}$, corrected for extinction and nebular emission contribution, and its uncertainty;

(40–47) ‘true’ colour indices $(U - B)_{\text{true}}$ (40), $(B - V)_{\text{true}}$ (42), $(V - R)_{\text{true}}$ (44), and $(V - I)_{\text{true}}$ (46), corrected for extinction and nebular emission contribution, and their uncertainties (41, 43, 45, 47);

(48, 49) the same as columns (19, 20), but corrected for extinction A , $I(\text{H}\alpha + [\text{N II}])$ ($I(\text{H}\alpha)$), and their uncertainties;

(50, 51) age t in units of Myr, and its uncertainty;

(52, 53) mass M in units of $10^4 M_{\odot}$, and its uncertainty;

(54) estimated diameter in units of pc;

(55) structure of the region [1 – separate object with a star-like profile, 2 – double object, 3 – triple object, 4 – separate object with a diffuse profile, 5 – ring structure, 6 – complex structure (more than three separate objects), 10...60 – the same as 1...6, but the object is a brighter part (core) of a more extended star-forming region].

We give the parameters of $\text{H}\alpha + [\text{N II}]$ ($\text{H}\alpha$) lines: F , F_0^i , I fluxes, and equivalent widths $\text{EW}(\text{H}\alpha)$ for all H II regions associated with stellar groupings, including cases where (i) the photometric radiation centre is displaced from the gas emission centre (class 1) and (ii) the gas emission is absent within the area of radiation from stars (class 0). At the same time, $R - \text{H}\alpha$ index was not calculated for the class 0 objects.

Gas metallicity Z is assumed to be equal to the metallicity of the stellar population for objects of any gas-to-stars morphology.

For the objects without $\text{H}\alpha$ emission within the area of radiation from stars (class 0), we assume $A(B) = A(B)_{\text{Gal}} + A(B)_{\text{in}}$.

The gas contribution $I_B(\text{gas})/I_B(\text{total})$ is assumed to be 0 for the class 0 objects.

In the catalogue, we present ‘true’ colours and absolute magnitudes only for objects of classes 2 and 0. In doing so, ‘true’ colours and absolute magnitudes for objects with absence of gas emission within the area of radiation from stars are equal to colours and magnitudes, corrected for the Galactic extinction and inclination effects. We did not calculate the colour index $(V - R)_{\text{true}}$ for stellar groupings with extremely high contribution of gas emission in the R band, $I_R(\text{gas})/I_R(\text{total}) > 0.4$.

Masses and ages of stellar groupings were estimated both for objects of classes 2 and 0. We did not include masses and (or) ages for some groupings, for which estimates of m and (or) t were obtained with low accuracy ($\Delta m/m \geq 1$, $\Delta t/t \geq 1$ if $t + \Delta t \leq 10$ Myr).

3.2 Physical parameters of stellar population in star formation regions

The completeness limits for object samples differ from galaxy to galaxy (Fig. 4), since the observations of galaxies were carried out with different telescopes and with different total exposures. In the most deeply exposed NGC 628 and NGC 6946, the sample is complete up to apparent B magnitudes of ≈ 22.0 and ≈ 21.7 mag, respectively (Fig. 4). The remaining galaxies in the sample were taken with lower exposures. The total distribution of 1510 stellar groupings has a maximum at ≈ 21.3 mag (Fig. 4). For galaxies with the worst signal-to-noise ratio, object samples are complete up to $m(B) \approx 20$ mag.

We constructed the luminosity function for stellar groupings in the galaxies with the largest numbers of identified star formation regions, NGC 628 and NGC 6946. We used a standard power-law luminosity function of the form

$$dN(L_{m(B)})/dL_{m(B)} = \beta L_{m(B)}^{\alpha}, \quad (2)$$

which was converted to the form

$$\log N = a \times m(B) + b \quad (3)$$

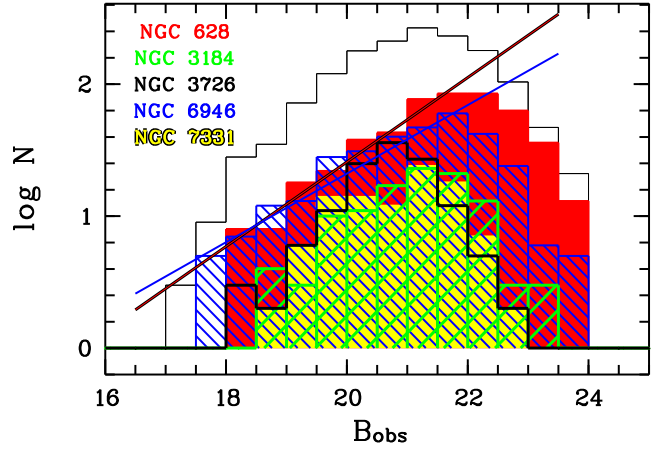


Figure 4. Luminosity functions for star formation regions using apparent B magnitude for our full sample (thin black), for objects in NGC 628 (red), NGC 3184 (green), NGC 3726 (thick black), NGC 6946 (blue), and NGC 7331 (yellow). Black-red-black and blue straight lines represent the power-law fit of the form of equation (3) for samples of star formation regions in NGC 628 and NGC 6946, respectively. See the text for details.

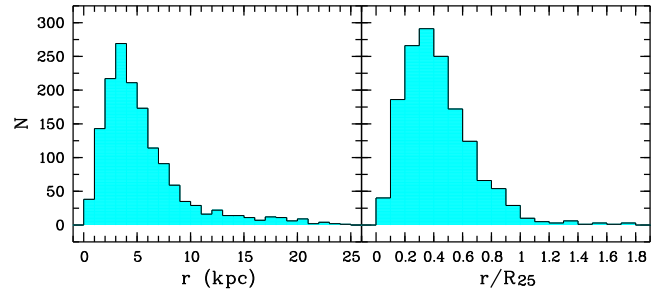


Figure 5. Distributions of studied star formation regions over their absolute galactocentric distances (left) and galactocentric distances normalized to the disc isophotal radius R_{25} of a galaxy (right) for 19 spiral galaxies under study.

for the fitting, where the variables α , β in equation (2) and a , b in equation (3) are related as $\alpha = -2.5a - 1$ and $\beta = 2.5(\ln 10)^{-1} 10^{b+4.8a}$, respectively.

The constructed star formation region luminosity functions are shown in Fig. 4. The luminosity functions have slopes $\alpha = -1.80 \pm 0.05$ for NGC 628 and $\alpha = -1.69 \pm 0.05$ for NGC 6946. These slopes are close to typical ones ~ -2 for H II regions and young open clusters in spiral galaxies (Larsen 2002; de Grijs & Anders 2006; Piskunov et al. 2006; Haas et al. 2008; Mora et al. 2009; Chandar et al. 2010; Whitmore et al. 2010; Baumgardt et al. 2013; Konstantopoulos et al. 2013; Fouesneau et al. 2014; Messa et al. 2018; Santoro et al. 2022). In particular, Santoro et al. (2022) obtained $\alpha = -1.7 \pm 0.1$ for H II regions in NGC 628 from the integral field spectroscopy (as part of PHANGS-MUSE survey; Emsellem et al. 2022), that is in agreement with our measurements based on the archival long-slit data.

Most of young stellar groupings are located, as expected, in regions of the developed spiral structure at galactocentric distances $0.1-0.7r/R_{25}$ (Fig. 5). At the same time, we identified 22 young objects at distances of $1.10-1.74r/R_{25}$. Six of them are located in the irregular galaxy NGC 5585. The remaining 16 are along the minor axis of the highly inclined disc of NGC 7721, and the accuracy of finding their galactocentric distances is low. We believe that the inclination of the disc of NGC 7721 (81°) is overestimated

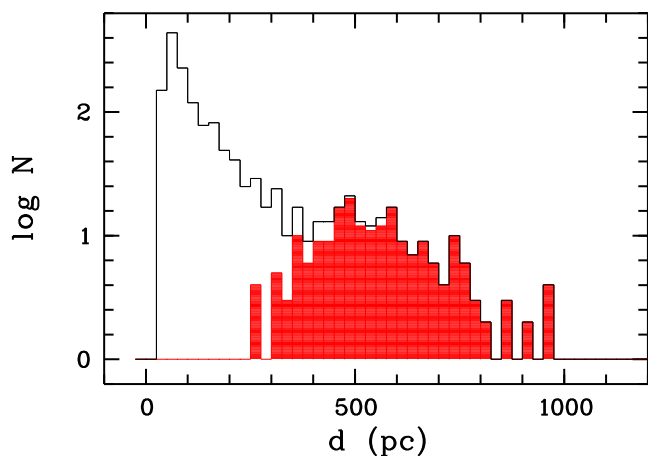


Figure 6. Distribution of studied star formation regions over their diameters. The red histogram shows the size distribution of objects in galaxies with distances $d > 30$ Mpc.

in the LEDA catalogue. The histogram of the distribution of stellar groupings by absolute distances to the centre (left-hand panel of Fig. 5) is similar in shape to the distribution in the right-hand panel of the figure. This is a consequence of the fact that four galaxies with the largest number of identified star-forming regions (NGC 628, NGC 3184, NGC 3726, and NGC 6946) have close sizes, their $R_{25} = 10.9\text{--}13.3$ kpc (see Table 1).

The size distribution of stellar groupings is strongly influenced by selection effects associated with the fact that the galaxies of our sample are located in a wide range of distances from the Milky Way. Among nearby galaxies ($d < 30$ Mpc), the size distribution of stellar groupings has a power-law form with a maximum at ≈ 70 pc (Fig. 6). Although resolution effects also play a role here, this diameter, 70 pc, is typical for stellar associations (Efremov, Ivanov & Nikolov 1987; Efremov 1989, 1995; Ivanov 1991; Efremov & Elmegreen 1998; Elmegreen 1994, 2009; Elmegreen & Efremov 1996; Odekon 2008; de la Fuente Marcos & de la Fuente Marcos 2009), and the power law of the size function for stellar associations and H II regions is well known (Elmegreen, Elmegreen & Leitner 2003a; Elmegreen et al. 2003b, 2006). In distant galaxies, where we cannot resolve individual associations, the size distribution has a maximum of $d = 500\text{--}600$ pc, which is a typical size of star complexes (Efremov 1995; Efremov & Elmegreen 1998; Elmegreen et al. 2000; Zhang, Fall & Whitmore 2001; Elmegreen 2002, 2011).

Gas in most of the studied H II regions has a sub-solar metallicity, $Z \sim 0.01 \simeq 0.55Z_{\odot}$ (Fig. 7). Because we had to use different empirical calibration methods (see Section 2.1.2), there are systematic discrepancies between the measured metallicity values. Whereas R, S, O3N2, and NS calibrations are in a good agreement with each other, H II-ChiMistry method gives, on average, 0.1–0.2 dex higher values of O/H (see the bottom panel of Fig. 7), close to solar ones.

We note, however, that errors in determining the chemical abundance have small effect on estimates of the age and mass of stellar groupings, since the difference in luminosities and colours for evolutionary sequences of different metallicities does not exceed the typical errors in the measured ‘true’ luminosities and colour indices of stellar groupings (see the sequences in the colour–magnitude and colour–colour diagrams below).

The radial distribution of the metallicities of H II regions in Fig. 7 shows a gradient, typical for discs of spiral galaxies (Pilyugin, Grebel & Kniazev 2014).

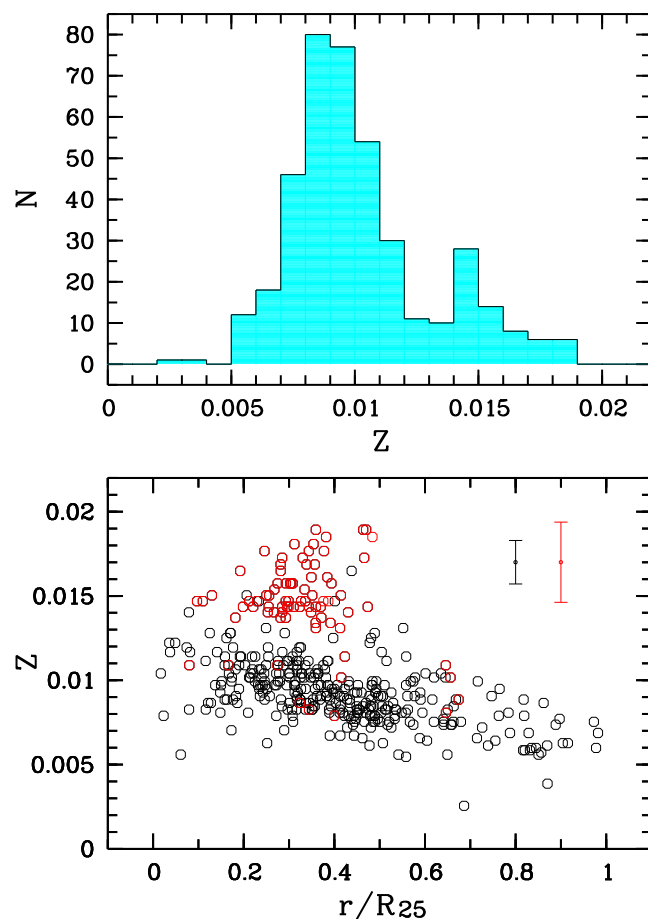


Figure 7. Metallicity distribution of star formation regions (top) and radial distribution of metallicities in discs of galaxies (bottom). H II regions, in which the abundances were measured with H II-ChiMistry method, are shown by red circles. Mean error bars are given. See the text for details.

Among the sample of our objects with available data in the H α line (1347 out of 1510), the majority (917 out of 1347, or 68 per cent) are star formation regions in which photometric (stellar) radiation centre is displaced from gas emission centre (class 1), 291 (22 per cent) objects are H II regions in which optical radiation from stars coincides with ionized gas emission (class 2), and 139 (10 per cent) objects have no gas emission within the area of optical radiation from stars (class 0; Fig. 8). Evolutionary classification scheme of Whitmore et al. (2011) predicts objects of class 1 to be between 4–5 and 8–10 Myr old, and objects of class 2 to be younger than 4–5 Myr. Taking into account that the youngest star formation regions with an age of 1–2 Myr are not visible in optics due to high extinction in the surrounding gas–dust cloud (e.g. Kim et al. 2021, 2023), as well as selection effects, due to which younger and dusty objects have a larger $m(B)$ than objects of class 1 of the same luminosity, a ratio of 3:1 for stellar groupings of class 1 and class 2 seems reasonable.

Spectral data are not available for the every object from our sample; therefore, we were able to obtain the Balmer decrement and estimate the extinction $A(B)$ in star formation regions only for 604 objects in the catalogue. We present in Fig. 9 the distribution of star formation regions by intrinsic extinction computed from Balmer decrement, $A(B)$, and corrected for the Galactic extinction and the dust extinction due to the inclination of a galaxy, $A(B)_{\text{Gal}} + A(B)_{\text{in}}$. Typical extinction $A(B) - A(B)_{\text{Gal}} - A(B)_{\text{in}} \approx 0.5$ mag in H II regions. For some regions, it can reach 4 mag, but usually does not exceed 2 mag (Fig. 9). Note

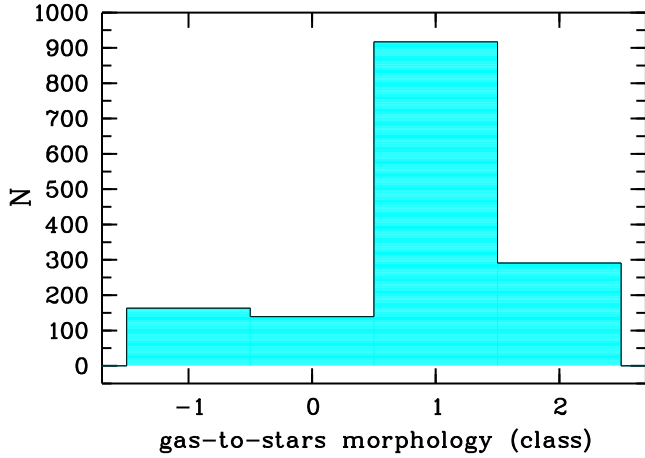


Figure 8. Distribution of studied star formation regions over their gas-to-stars morphology. See the description of the catalogue’s column (28) in Section 3.1 for details.

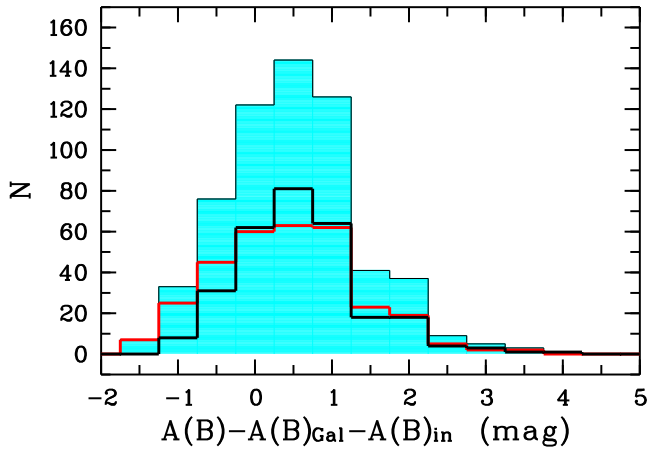


Figure 9. Frequency distribution of star formation regions over intrinsic extinction within the star formation regions for objects of all classes (cyan), for objects of class 2 (black), and for objects of class 1 (red). Intrinsic extinction within the star formation region is determined as a difference between the extinction found from Balmer decrement, $A(B)$, and sum of the Galactic extinction and the dust extinction due to the inclination of a galaxy, $A(B)_{\text{Gal}} + A(B)_{\text{in}}$. See the text for details.

that among the regions, for which the Balmer decrement $A(B) < A(B)_{\text{Gal}} + A(B)_{\text{in}}$, the regions with a displaced gas emission centre (class 1) dominate. Among the regions of class 2, we found only 47 objects (16 per cent), in which the negative $A(B) - A(B)_{\text{Gal}} - A(B)_{\text{in}}$ exceeds the errors $\Delta A(B)$. Note that the mean $\Delta A(B) = 0.26$ mag for class 2 objects and 0.32 mag for class 1 objects.

Negative $A(B) - A(B)_{\text{Gal}} - A(B)_{\text{in}}$, as a rule, are not the result of errors in spectroscopic measurements. $A(B)_{\text{in}}$ is the average value for the galaxy as a whole. However, extinction in a galaxy is not a constant value, it has radial and vertical gradients, as well as local variations. Therefore, $A(B)_{\text{in}}$ for a particular cluster depends on its galactocentric distance and vertical distance from the disc plane. It may be less than the average for the galaxy as a whole.

We note specific cases when the $A(B)_{\text{Gal}}$ extinction can also differ from the average for an extragalactic cluster. An example is the galaxy NGC 6946 (see Table 1), located at a low Galactic latitude ($b = 11.7^\circ$). Small local changes in extinction in the Milky Way

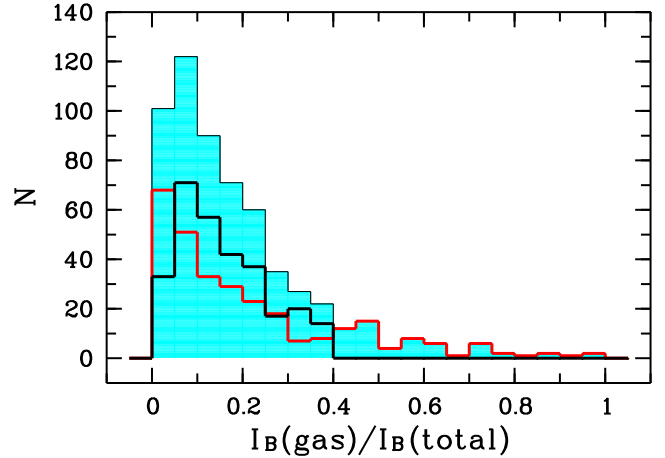


Figure 10. Distributions of studied star formation regions over nebular emission contribution in the B band. The symbols are the same as in Fig. 9.

can give significant deviations of $A(B)_{\text{Gal}}$ over the field of the galaxy (Efremov, Afanasiev & Egorov 2011).

The distribution of objects by gas emission contribution to the total radiation in photometric broad-bands is similar to what we obtained in Gusev et al. (2016) in fig. 11. The characteristic nebular contribution in the B band is about 10 per cent (Fig. 10). Among regions of class 1, a relative excess of objects with small (< 5 per cent) and large (> 40 per cent) nebular contributions is observed. Apparently, in the first case, we have spectral observations, in which the slit passed through the photometric (stellar) centre of H II region, and in the second case, it passed through the centre of gas emission.

We present a colour–magnitude diagram $B - V$ versus $M(B)$ for the ‘true’ colours and luminosities of stellar population of the studied star formation regions of classes 0 and 2, as well as open star clusters in the Milky Way from the catalogue of Kharchenko et al. (2005a, b, 2009) in Fig. 11. As can be seen from the figure, the vast majority of objects are well described by synthetic evolutionary SSP sequences for continuously and randomly populated IMF.

Note that among young stellar groupings without H α emission (class 0) there are no high-mass objects with $M > 2 \times 10^5 M_\odot$. The reason for this phenomenon will be discussed in Section 4.

Fig. 11 shows that the brightest open star clusters in our Galaxy and the dimmest stellar groupings from our sample are superimposed on each other in the colour–magnitude diagram. This confirms the conclusion of Gusev et al. (2016) that extragalactic young stellar groupings and open star clusters in the Milky Way form a continuous sequence of masses and ages and they represent a single evolutionary sequence of objects at different stages of their evolution.

We present colour–colour diagrams of colour indices, corrected for the Galactic extinction and the dust extinction due to the inclination of a galaxy, for all objects of our sample in Fig. 12. As can be seen from the figure, most of the star formation regions are well superimposed on the evolutionary sequences of young stellar systems with $t \leq 10$ Myr. The exception is the $(B - V)_0^i - (V - R)_0^i$ diagram, where a ‘tail’ of objects with an anomalously large $(V - R)_0^i$ is observed. The excess radiation in the R band is due to the large contribution of gas emission lines to this photometric band.

The star formation regions with no gas emission (class 0) and the regions, for which there are no H α data, lie more compactly along the evolutionary sequences on the colour–colour diagrams, than the regions with the presence of H α emission (classes 1 and 2). This is due to selection effects: objects without gas emission were

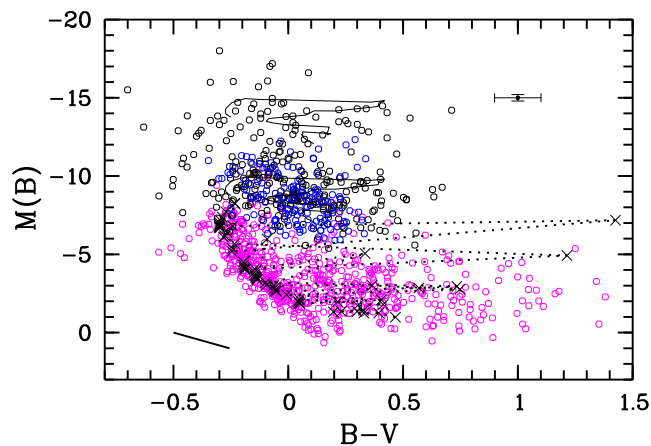


Figure 11. True colours and luminosities of studied young stellar groupings (black and blue open circles) and open clusters in the Milky Way (magenta open circles) compared with the *Standard* mode of SSP models (continuously populated IMF; black curves) and the *Extended* SSP mode (randomly populated IMF; black crosses connected by dotted lines). The objects of class 2 are indicated by black, and the objects of class 0 are shown by blue. Mean error bar is given. Two evolutionary sequences of the *Standard* mode with an adopted characteristic metallicity of $Z = 0.008$, drawn in the age interval from 1 to 100 Myr are shown. The sequences were computed for the masses of star clusters of 1×10^6 and $1 \times 10^4 M_{\odot}$. The sample of *Extended* SSP models with randomly populated IMF generated for the characteristic metallicity of galactic open clusters ($Z = 0.019$), shown with crosses connected by dotted lines in order of increasing age, demonstrates the evolutionary sequence for $500 M_{\odot}$ in the age range of 1 Myr to 1 Gyr.

selected based only on their colour indices $(U - B)_0^i$ and $(B - V)_0^i$ (see Section 2.2). The largest scatter in the colour–colour diagrams is observed for regions with displaced gas emission centre (class 1), because the gas emission contribution and ‘true’ (Balmer) absorption in the H II region are not taken into account here.

On colour–colour diagrams showing the ‘true’ colours of stellar groupings (Fig. 13), objects are located more compactly along evolutionary sequences than the star formation regions in the diagrams $(U - B)_0^i - (B - V)_0^i$, $(B - V)_0^i - (V - R)_0^i$, and $(B - V)_0^i - (V - I)_0^i$ (Fig. 12). This may indicate the correctness of our estimates of the nebular emission contribution and extinction calculated from the Balmer decrement.

Part of stellar groupings of class 2 with $(B - V)_{\text{stars}} \sim 0.4$ and $(U - B)_{\text{stars}} > 0$ is well described only by evolutionary sequences with a randomly populated IMF in the $(U - B) - (B - V)$ diagram. In the $(U - B)_0^i - (B - V)_0^i$ diagram, there are no star formation regions with such $(U - B)_0^i$ and $(B - V)_0^i$ (Fig. 12).

Stellar groupings with gas emission (class 2) have systematically smaller colour indices $U - B$ and $B - V$ than regions without gas emission (class 0). This is especially clearly seen in the $(U - B) - (B - V)$ diagram (Fig. 13). This is an expected result, reflecting the fact that star formation regions with gas emission should be younger and bluer on average.

Among 430 stellar groupings of classes 0 and 2, we were able to estimate the mass for 409 and the age for 391 objects using evolutionary models. Most star clusters have masses in the range of $3 \times 10^3 - 3 \times 10^5 M_{\odot}$ (Fig. 14). Two-thirds of stellar groupings can be attributed to massive star clusters with $M > 1 \times 10^4 M_{\odot}$. The minimum masses were fixed for stellar groupings no. 465 in NGC 628 ($430 M_{\odot}$) and nos. 286, 301, 367 in NGC 628, and no. 634 in NGC 3184 ($790 M_{\odot}$). According to our estimates, stellar complexes

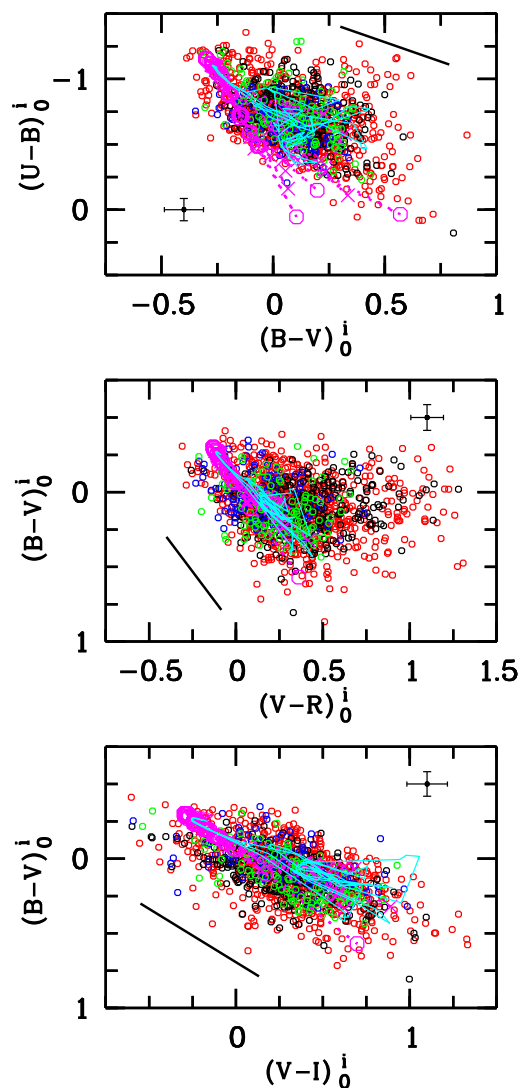


Figure 12. Colour–colour diagrams $(U - B)_0^i - (B - V)_0^i$, $(B - V)_0^i - (V - R)_0^i$, and $(B - V)_0^i - (V - I)_0^i$ for star formation regions of different gas-to-stars morphology. The class 2 objects are shown by black, the class 1 objects are given by red, the class 0 objects are indicated by blue, and the objects with no H α data are shown by green. The colour indices are corrected for the Galactic extinction and the dust extinction due to the inclination of a galaxy. Mean error bars are given. The black straight line in the corner of the diagrams is parallel to the extinction vector. Cyan curves show SSP models with continuously populated IMF with $Z = 0.008, 0.012,$ and 0.018 for the age interval from 1 to 100 Myr. Circles and crosses connected by magenta dotted lines, in order of increasing age, indicate two samples of *Extended* SSP models with randomly populated IMF with $Z = 0.008$ generated for star cluster masses $5 \times 10^3 M_{\odot}$ (crosses) and $500 M_{\odot}$ (circles) in the age range of 1 Myr to 1 Gyr.

no. 1439 in NGC 7678 and no. 890 in NGC 5351 have the maximum masses (3×10^7 and $1.3 \times 10^7 M_{\odot}$, respectively).

As noted above, among the objects without gas emission (class 0) there are no high massive star complexes with $M > 2.2 \cdot 10^5 M_{\odot}$. We also did not find stellar groupings of class 0 with masses $M < 1.1 \cdot 10^3 M_{\odot}$ (Fig. 14).

The age range of stellar groupings turned out to be unexpectedly wide: from 1 to 560 Myr (Fig. 15). 154 regions (39 per cent) are younger than 10 Myr, another 137 objects (35 per cent) have an age of 10–25 Myr.

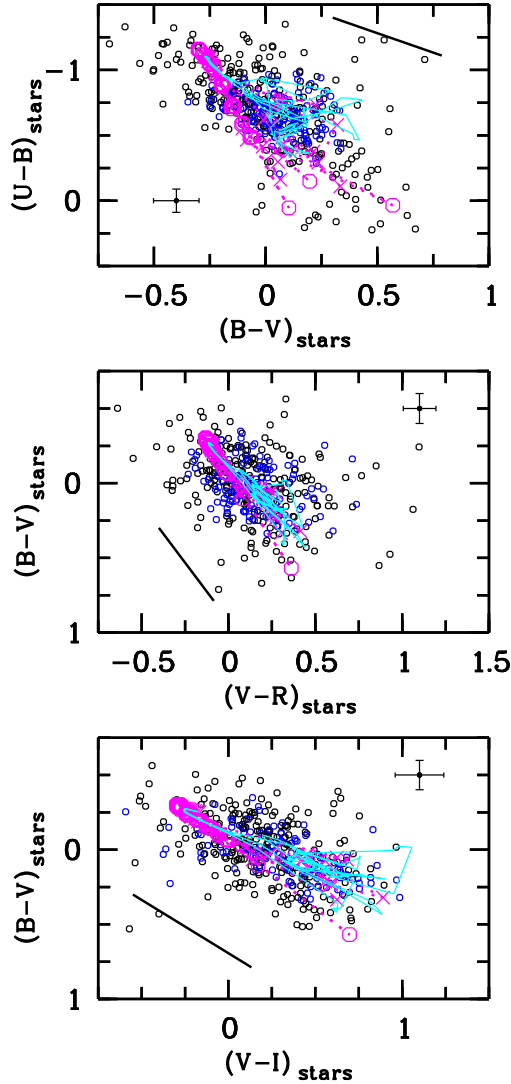


Figure 13. Colour–colour diagrams $(U - B) - (B - V)$, $(B - V) - (V - R)$, and $(B - V) - (V - I)$ for true colours of studied young stellar groupings. The class 2 objects are shown by black open circles and the class 0 objects are indicated by blue open circles. Other symbols are the same as in Fig. 12.

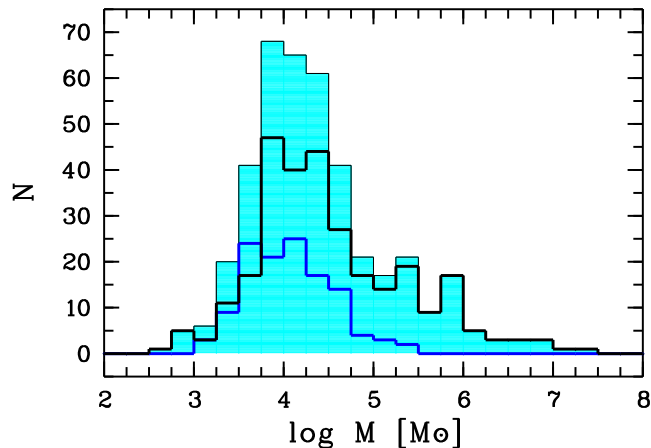


Figure 14. Frequency distribution of stellar groupings over mass for all regions (cyan), for class 2 objects (black), and for class 0 objects (blue).

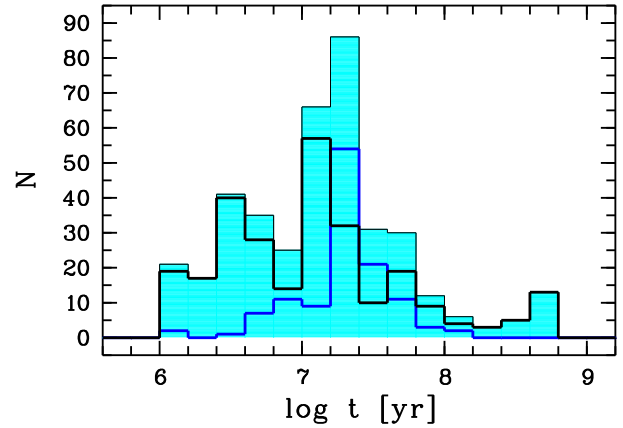


Figure 15. Frequency distribution of stellar groupings over age. The symbols are the same as in Fig. 14.

Objects without gas emission (class 0), as expected, turned out to be on average older than regions with $H\alpha$ emission. The boundary, at which regions of class 0 begin to predominate, is the age of 15–16 Myr (Fig. 15). Objects without $H\alpha$ emission are practically absent among very young ($t < 4$ Myr) and relatively old ($t > 130$ Myr) stellar groupings (Fig. 15). A probable reason for the presence of gas emission in stellar groupings older than 10 Myr is prolonged or multiburst star formation, which is poorly described in terms of SSP evolutionary models (see Section 4 for details).

In order to verify that the measured properties of the ionized gas and stars presented in our catalogue are consistent with what is typically observed in nearby galaxies by other authors, we compare their distribution to what is derived from PHANGS-MUSE (Emmellem et al. 2022) and PHANGS-*HST* (Lee et al. 2022) data. Within PHANGS survey, 19 nearby galaxies were mapped with MUSE and 38 galaxies with *HST*, while only one galaxy (NGC 628) is also in our catalogue. From these data, the properties of about 30 000 $H\text{ II}$ regions (Groves et al. 2023) and about 100 000 young compact star clusters (Whitmore et al. 2021; Thilker et al. 2022) and OB associations (Larson et al. 2023) were derived, and currently the corresponding catalogues are ones of the most comprehensive sources of the resolved observational properties of the $H\text{ II}$ regions and star clusters in nearby galaxies. In Fig. 16, we show the distribution of the gas-phase oxygen abundances, $\text{EW}(H\alpha)$, total stellar mass and age of the star groupings in our study (blue histograms), and those taken from the PHANGS catalogues (orange histogram) derived from the MUSE (for oxygen abundance and equivalent width) and *HST* (for stellar mass and age) observations. As follows from these plots, the regions from our catalogue cover roughly the same range of metallicities and stellar masses, although the PHANGS-*HST* data are more sensitive and complete at the low-mass range of star clusters. The fraction of the relatively old star clusters is significantly higher in our sample, probably due to the fact that we are studying the larger stellar groupings (thus their average age can be older than the age of the youngest individual compact clusters there), while PHANGS-*HST* resolves more compact star clusters and young stellar associations. Finally, the values of $\text{EW}(H\alpha)$ measured for our sample are slightly lower than for PHANGS-MUSE $H\text{ II}$ regions. We note here that the latter values were corrected for contamination by background old stellar population, which is quite strong in the IFU data like PHANGS-MUSE. Scheuermann et al. (2023) showed that background-corrected values of $\text{EW}(H\alpha)$ from PHANGS-MUSE

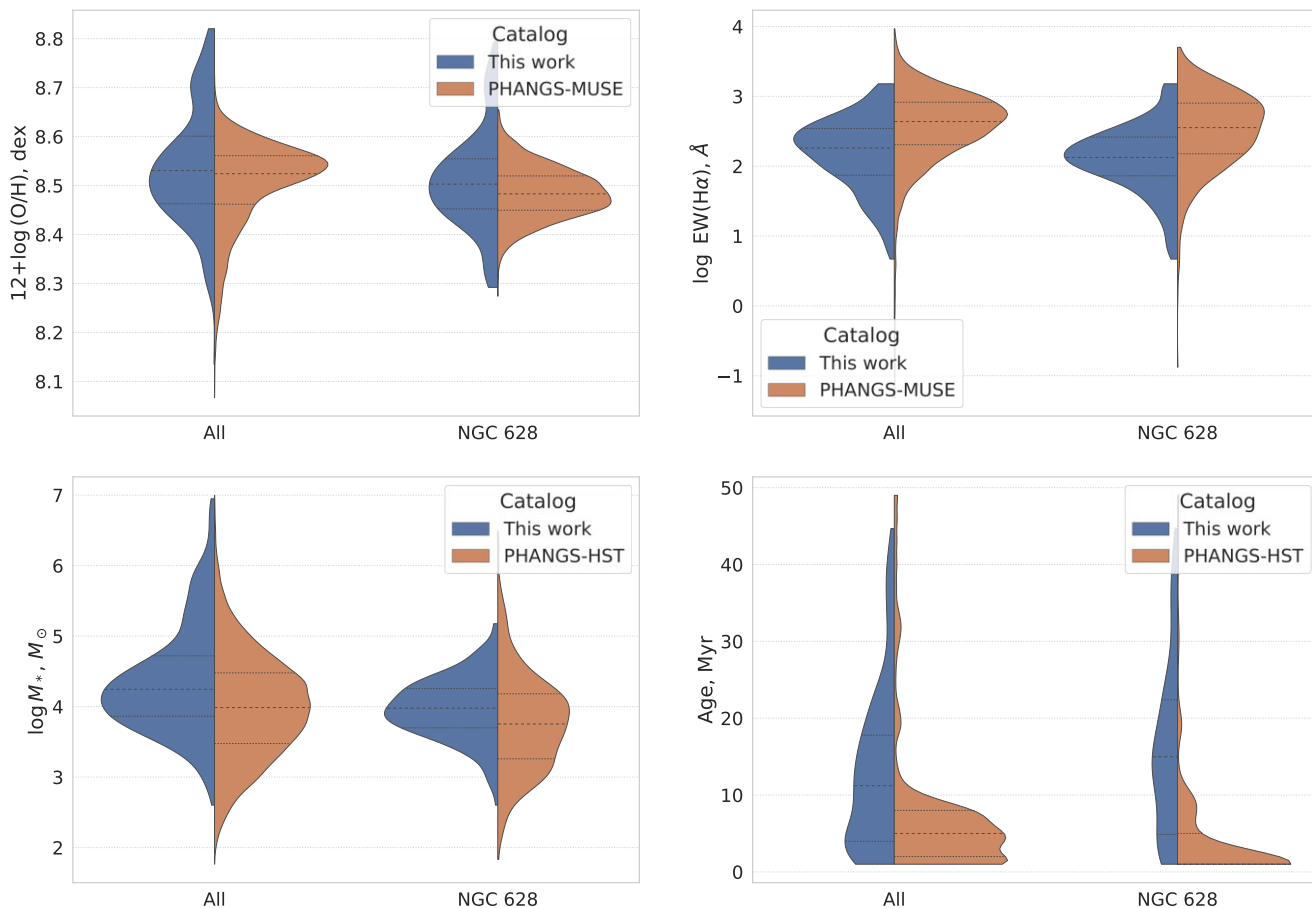


Figure 16. Distribution of the gas-phase oxygen abundance (top-left panel), equivalent width of H α line (top-right panel), stellar mass (bottom-left panel), and age (bottom-right panel) derived for stellar groupings from this study (blue colour) in comparison to the distribution of the same parameters for H II regions and compact star clusters and young associations for the sample of other nearby galaxies from the PHANGS survey based on MUSE and *HST* observations (taken from the catalogues by Whitmore et al. 2021; Thilker et al. 2022; Groves et al. 2023; Larson et al. 2023). The right-hand set of histograms on each plot shows the distribution for NGC 628 – the only overlapping object in our samples. The values of EW(H α) from PHANGS-MUSE were corrected for the background old stellar population, while no such correction was performed for our sample (see the text).

catalogue are about an order of magnitude larger than the observed ones, and in Fig. 16 we show the corrected values from that paper. Our measurements rely mostly on the long-slit data and less suffer from this effect, although slight displacement between the distributions can be due to the fact that we did not perform such correction for our measurements (but also due to in general older ages of the stellar population).

4 DISCUSSION

The duration of star formation is approximately proportional to the mass of a molecular cloud and a star grouping formed from it. Star formation in massive star complexes lasts ~ 20 Myr (Efremov & Elmegreen 1998). Probably, in the most massive star complexes, we observe the emission of hydrogen from the last, recent starburst. At the same time, the first starburst could have occurred relatively long ago. In the absence of a recent burst of star formation, the colour indices of such complexes are not well defined by SSP models as several generations of stars could be observed at the same place. Therefore, we have not identified any star complexes without gas emission (class 0) with a mass $M > 2.2 \times 10^5 M_{\odot}$ (see Figs 11 and 14).

The relative duration of star formation in large star complexes can also explain the fact that there are no low-mass stellar systems ($M < 10^4 M_{\odot}$) among the ‘oldest’ stellar groupings ($t > 130$ Myr) of any classes (2 and 0).

As we noted in Section 1, EW(H α) appears to be one of the commonly used age indicators. The definite advantage of this indicator is its insensitivity to the interstellar extinction. In Fig. 17, we compare EW(H α) to the $R - H\alpha$ index (also independent on reddening) that we introduced in Section 3.1. From the definition of the index, $\log \text{EW}(\text{H}\alpha) \sim 0.4(R - H\alpha)$, and the meaning of that index is the same as of EW(H α) assuming the underlying stellar continuum has a flat shape. Formally found linear regression coefficient between these two indexes for the considered star formation groupings is equal to 0.407, very close to 0.4. The resulting relation between the indexes can be described as

$$\log \text{EW}(\text{H}\alpha) = 0.4(R - H\alpha) + (8.5 \pm 0.3). \quad (4)$$

However, the scatter in Fig. 17 and the derived uncertainties of the offset in equation (4) (± 0.3 dex) do not allow its accurate application to the real data. In particular, there is a numerous group of H II regions, mostly of class 1, with anomalously low EW(H α) for a given $R -$

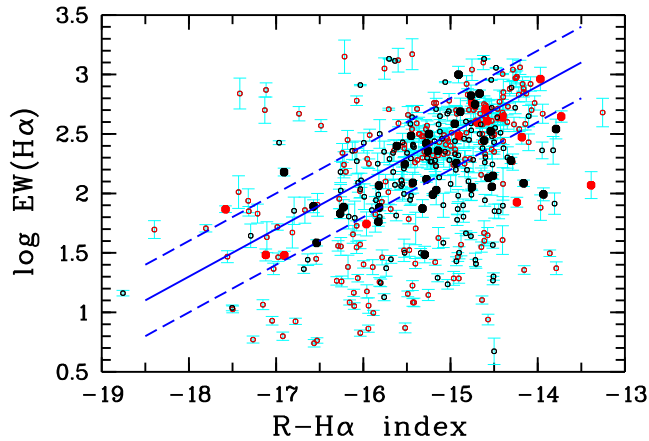


Figure 17. $R - H\alpha$ index versus $\log EW(H\alpha)$ diagram for star formation regions of class 2 (open black circles) and class 1 (open red circles) with $\Delta \log EW(H\alpha) < 0.15$ dex. Our objects from Gusev et al. (2016) are shown as large filled circles. Error bars are given. The solid line is a linear fit from equation (4). Dashed lines are upper and lower 1σ errors of $\log EW(H\alpha)$ from equation (4).

$H\alpha$ index (Fig. 17). Note that the mean error $\Delta \log EW(H\alpha)$ is equal to 0.06 dex for the objects in Fig. 17.

Analysing the $EW(H\alpha)$, obtained by different authors for the same $H II$ regions, we found that the differences in the measured $EW(H\alpha)$ can reach a factor of 2–3. This is also why, after averaging (see Section 2.1.2), the $EW(H\alpha)$ errors in Fig. 17 and in the catalogue turned out to be larger than the $EW(H\alpha)$ errors of individual measurements.

In our opinion, there are two main reasons for the large scatter in $EW(H\alpha)$ measurements. The first one is related to the fact that the $EW(H\alpha)$ values are sensitive to the choice of the background area (continuum from the underlying stellar disc). Small changes in the continuum under the $H\alpha$ line lead to significant changes in the $EW(H\alpha)$ value. The second reason, which is specific for slit spectroscopy, is related to the fact that different parts of $H II$ region with different $EW(H\alpha)$ can fall into the slit. Additional reasons for the scatter in $EW(H\alpha)$ measurements can be also due to variations of the filling factors in $H II$ regions and the fraction of ionizing photons which escape from the nebulae. Therefore, the use of $EW(H\alpha)$ as an age indicator in $H II$ regions should be treated with caution.

We plotted the age versus $EW(H\alpha)$ and the age versus $R - H\alpha$ index diagrams in Fig. 18 for the objects with the most precisely measured $EW(H\alpha)$ and t . STARBURST99 evolutionary models (Leitherer et al. 1999) show that $EW(H\alpha)$ in $H II$ regions decreases from $>1000 \text{ \AA}$ in the youngest star clusters to $\approx 30\text{--}40 \text{ \AA}$ in the regions with an age of 10 Myr (Reines et al. 2010). The lowest $EW(H\alpha)$ values for a given age in Fig. 18 correspond to those predicted by STARBURST99 models, however, the largest values ($\sim 1000 \text{ \AA}$) are found for young stellar regions of all ages, up to $t = 17$ Myr.

A similar picture is observed in the age versus $R - H\alpha$ index diagram: excluding the youngest regions with $t \approx 1$ Myr, the minimum values of the index fall from -15 to -18 in the age range of 3–15 Myr, while the maximum indices remain constant, $R - H\alpha = -14$ (Fig. 18).

Apparently, the lack of a strong correlation between age and $EW(H\alpha)$ predicted by evolutionary models is due to the complex star formation history in the $H II$ regions, which is poorly described by SSP models. This is also indicated by the fact that there are

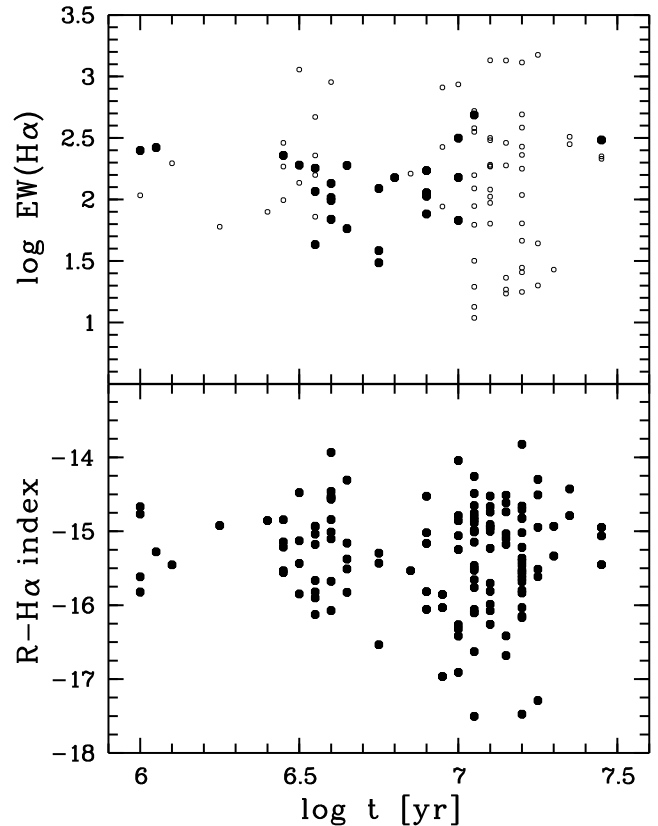


Figure 18. Age versus $\log EW(H\alpha)$ (top) and age versus $R - H\alpha$ index (bottom) diagrams for the most accurately measured star formation regions [$\Delta \log EW(H\alpha) < 0.15$ dex for the objects in the top panel and $\Delta \log t < 0.2$ dex]. Symbols in the top panel are the same as in Fig. 17. See the text for details.

no objects with a low $R - H\alpha$ index (< -16.5) among young low massive ($M < 10^4 M_\odot$) stellar groupings.

At the same time, we believe that the introduced $R - H\alpha$ index can be used when $EW(H\alpha)$ is not available because of absence of spectral observations of star formation regions for their analysis. Given the weakness of the correlation with the age of the regions derived from SED fitting, one cannot rely on either of these indexes for the precise age-dating based without properly addressing two most probable sources of the scatter mentioned above (contamination by the background stellar population, uncertainties in the escape fraction of the ionizing quanta and the differences in the area covered by the aperture). Integral field spectroscopy is necessary to overcome some of such limitations related to the incomplete coverage of $H II$ region. However, even then the measured values $EW(H\alpha)$ often disagree with those predicted from models (e.g. Morisset et al. 2016; Kreckel et al. 2022) and only weakly correlate with the stellar association ages measured from SED fitting (e.g. Scheuermann et al. 2023).

Our sample contains various types of young stellar objects: OB associations, open clusters, stellar aggregates, and star complexes. Their dynamic evolution is different. Large stellar aggregates with sizes >150 pc and star complexes with $d \approx 500\text{--}600$ pc have a complex structure and contain conglomerates of star clusters and associations. $H II$ regions and associations may expand with age inside the complex, but the size of the complex depends fundamentally on the physical parameters of the surrounding interstellar matter and the magnetic field (Elmegreen et al. 2003a; Elmegreen et al. 2003b; Gusev & Efremov 2013).

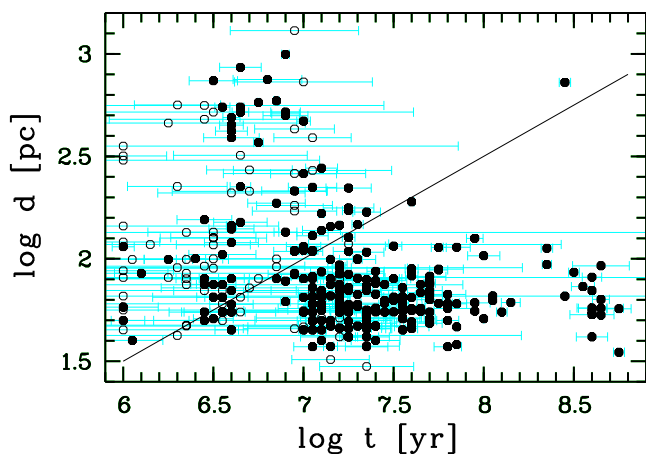


Figure 19. The age versus size diagram for stellar groupings. Objects with $\Delta \log t < 0.2$ dex are indicated by filled circles. The solid line represents the dependence $t \sim d^2$. Error bars are shown. See the text for details.

Modern high-resolution studies using *HST* data of resolved H II regions show that the size of an H II region is a function of the age of the stellar population (Whitmore et al. 2011; Kim et al. 2012). However, this dependence is observed up to an age of 5–6 Myr and a diameter of 40 pc. The sizes of H II regions (future star clusters) starting from 40 pc weakly depend on the age of the stellar population (Whitmore et al. 2011). However, the ‘age–size’ relation is observed for star associations over a wider range of ages and sizes (Efremov & Elmegreen 1998; Portegies Zwart et al. 2010). Unfortunately, as we noted in Section 1, the youngest ($t \leq 10$ Myr) clusters and associations are poorly differentiated by their parameters (Gieles & Portegies Zwart 2011), and the minimum linear resolution of our observations is 30–40 pc in the nearest galaxies.

Fig. 19 illustrates the dependence between the age and the size of the studied stellar groupings. To make a homogeneous sample, multiple (double, triple, and complex) objects have been excluded from the graph [see comments for column (55) of the catalogue]. Visually, we do not find any correlation between the age and the size of the young stellar groupings in the figure. However, we can separate large star complexes, a few stellar aggregates, and numerous star clusters. They vary in size but do not show ‘age–size’ dependence. However, the distribution of young ($t < 10$ Myr) small ($d < 120$ pc) stellar groupings on the graph seems to indicate the presence of the ‘age–size’ relation. Larger star associations are older. A diffusion-driven expansion, which produces a relation $t \sim d^2$ between age and size, seems to play the main role here (see Fig. 19).

A correlation between sizes and masses of GMCs, $M \sim d^2$, was found for the first time by Larson (1981). That correlation has been repeatedly confirmed later (see e.g. Hopkins 2012). The mass–size relation for young star complexes was found to be close to that of GMCs, (see Adamo et al. 2013, and references therein). It reflects the fact that young star complexes are the direct descendants of GMCs. Using the GMC sample of Bolatto et al. (2008) and their own sample of young massive clusters, Adamo et al. (2013) gave a relation $M \sim d^{2.0 \pm 0.3}$ for young star complexes and $M \sim d^{1.9 \pm 0.1}$ for GMCs (see Fig. 20). However, more recent studies of star clusters and GMCs have shown more complex relations between their masses and sizes (see e.g. compilation in Grudić et al. 2021).

The dependence between sizes and masses of stellar groupings from our sample is presented in Fig. 20. As in the ‘age–size’ diagram (Fig. 19), we excluded multiple objects from the graph. We also

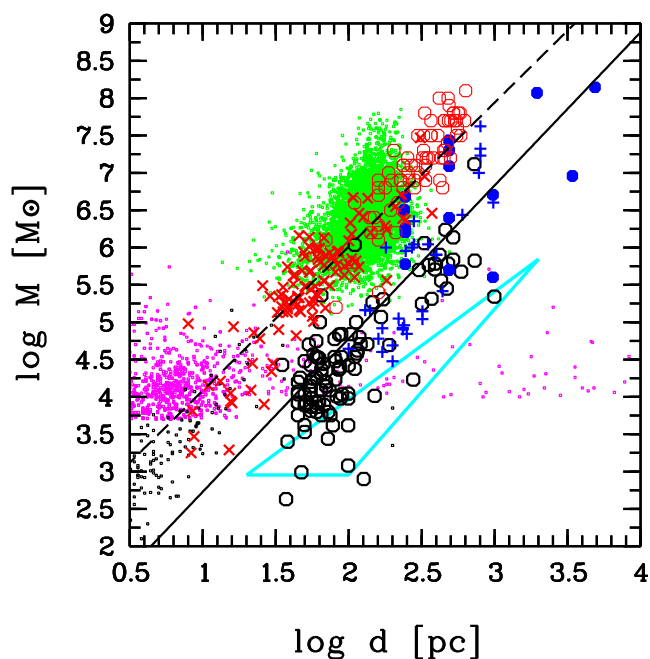


Figure 20. Size versus mass diagram for stellar groupings from our sample with $\Delta M/M < 0.2$ (black open circles), young massive cluster complexes in the very distant ($z \sim 1.5$) galaxy Sp 1149 (blue filled circles) and cluster complexes in the local galaxies (blue crosses) by Adamo et al. (2013), young star clusters in NGC 628, NGC 1313, and NGC 5236 (Ryon et al. 2015, 2017) (magenta dots), Small Magellanic Cloud star clusters (Gatto et al. 2021) (black dots), stellar conglomerations in NGC 1566 (Gouliermis et al. 2017) (area inside the cyan triangle), giant molecular clouds from Bolatto et al. (2008) (red crosses), Wei, Keto & Ho (2012) (red open circles), and Rosolowsky et al. (2021) (green dots). The solid line is a linear fit, computed for local and high- z young massive complexes in Adamo et al. (2013). The dashed line is a linear fit, computed for giant molecular clouds from the Bolatto et al. (2008) sample. Mass measurement error bars for our objects are smaller than circle sizes in the figure. See the text for details.

excluded objects with mass estimation errors > 20 per cent. The stellar groupings from our sample are in fairly good agreement with the dependence $M \sim d^2$ obtained by Adamo et al. (2013) for the size range from 50 to 1000 pc (Fig. 20). Note that small stellar groupings ($d = 50$ –100 pc) also fit well with the ‘size–mass’ dependence (Adamo et al. (2013) studied star clusters larger than 100 pc. At the same time, our data also agree well with the results of Gouliermis et al. (2017) for stellar conglomerations with the highest surface brightness from their sample (upper side of the cyan triangle in the figure).

The ‘size–mass’ relation which is observed for star clusters, associations and complexes is a relic of the same dependence for their ancestors, the GMCs. The vertical shift between the GMCs and the stellar groupings in the diagram is due to the star formation efficiency: only a fraction of the gas in the GMCs will form stars (Bastian et al. 2005; Adamo et al. 2013). The width of the band occupied by stellar groupings along the dependence line $M \sim d^2$ testifies to the differing efficiency of star formation in different regions, which is usually 1–7 per cent.

5 CONCLUSIONS

In this paper, we present the results of analysis of the catalogue comprising parameters of 1510 young stellar groupings. This cat-

atalogue is based on the combination of spectroscopic, photometric, and H α spectrophotometric data for star formation regions in 19 galaxies. We have studied the morphology of stellar groupings and their relation to the associated H α emission region. Extinctions for 743, metallicities for 402, ages for 391, and masses for 409 stellar groupings were estimated.

We used a continuously populated IMF for high massive clusters ($M > 1 \times 10^4 M_{\odot}$) and a randomly populated IMF for star clusters with $M < 1 \times 10^4 M_{\odot}$ in the evolutionary synthesis models to estimate ages and masses of stellar groupings.

It is shown, that the method we use for estimating the age and mass of the stellar component in star formation regions is applicable only for objects, in which the optical radiation from stars coincides with the ionized gas emission and for objects without gas emission within the area of optical radiation from stars. Note that the number of regions with a displacement between the centres of gas emission and photometric (stellar) radiation is three times greater than the number of regions where the optical radiation from stars coincides with the gas emission.

The derived masses of stellar groupings range from 430 M_{\odot} in the nearby galaxy NGC 628 to $3 \times 10^7 M_{\odot}$ in the distant NGC 7678. Most stellar groupings have masses in the range of 3×10^3 – $3 \times 10^5 M_{\odot}$. Two-thirds of stellar groupings can be attributed to massive star clusters with $M > 1 \times 10^4 M_{\odot}$.

The range of ages of stellar groupings is from 1 to 560 Myr. One-third of regions are younger than 10 Myr, and another one-third of objects has an age of 10–25 Myr. The age boundary, at which regions without gas emission begin to predominate over objects with H α emission, is 15–16 Myr.

The lower mass estimates for the regions in NGC 628, NGC 3184, and NGC 6946 overlaps with the mass interval of the young Milky Way open clusters. This is an argument for the existence of a uniform evolutionary sequence of extragalactic star formation regions and Galactic open clusters at different stages of their evolution.

The introduced $R - H\alpha$ index = $R + 2.5 \log F(H\alpha + [N II])$ can be used when EW(H α) is not available because of absence of spectral observations of star formation regions for their analysis.

ACKNOWLEDGEMENTS

We are extremely grateful to the anonymous referee for his/her helpful and constructive comments. The authors would like to thank A. E. Piskunov (Institute of Astronomy of Russian Academy of Sciences) for helpful consultations. The authors acknowledge the use of the HyperLeda data base (<http://leda.univ-lyon1.fr>), the NASA/IPAC Extragalactic Database (<http://ned.ipac.caltech.edu>), Strasbourg Astronomical Data Center (CDS, <https://cds.u-strasbg.fr>), the Sloan Digital Sky Survey (SDSS, <http://www.sdss.org>), the Padova group online server CMD (<http://stev.oapd.inaf.it>), the European Southern Observatory Munich Image Data Analysis System (ESO-MIDAS, <http://www.eso.org/sci/software/esomididas>), and SEXTRACTOR programme (<http://sextractor.sourceforge.net>). This study was supported by the Russian Foundation for Basic Research (project no. 20-02-00080). This research has been supported by the Interdisciplinary Scientific and Educational School of Moscow University ‘Fundamental and Applied Space Research’.

DATA AVAILABILITY

The catalogue is presented as the additional online material to this paper in the MNRAS website. It is also available in electronic form at http://lnfm1.sai.msu.ru/~gusev/sfr_cat.html. Some of the images are

available in NASA/IPAC Extragalactic Database at <http://ned.ipac.caltech.edu>. Spectral data are available in the Sloan Digital Sky Survey at <http://www.sdss.org>, Strasbourg Astronomical Data Center at <https://cds.u-strasbg.fr>, or in corresponding papers. Our own *UBVRI* and H α observational data can be shared on reasonable request to the corresponding author.

REFERENCES

- Adamo A., Östlin G., Bastian N., Zackrisson E., Livermore R. C., Guaita L., 2013, *ApJ*, 766, 105
- Adamo A. et al., 2017, *ApJ*, 841, 131
- Albaret F. D. et al., 2017, *ApJS*, 233, A25
- Artamonov B. P., Bruevich V. V., Gusev A. S., 1997, *Astron. Rep.*, 41, 577
- Artamonov B. P., Badan Y. Y., Bruevich V. V., Gusev A. S., 1999, *Astron. Rep.*, 43, 377
- Artamonov B. P., Badan Y. Y., Gusev A. S., 2000, *Astron. Rep.*, 44, 569
- Bastian N., Gieles M., Efremov Y. N., Lamers H. J. G. L. M., 2005, *A&A*, 443, 79
- Bastian N., Emsellem E., Kissler-Patig M., Maraston C., 2006, *A&A*, 445, 471
- Bastian N., Tranco G., Konstantopoulos I. S., Miller B. W., 2009, *ApJ*, 701, 607
- Baumgardt H., Parmentier G., Anders P., Grebel E. K., 2013, *MNRAS*, 430, 676
- Belley J., Roy J.-R., 1992, *ApJS*, 78, 61
- Berg D. A., Skillman E. D., Garnett D. R., Croxall K. V., Marble A. R., Smith J. D., Gordon K., Kennicutt R. C., Jr, 2013, *ApJ*, 775, A128
- Berg D. A., Skillman E. D., Croxall K. V., Pogge R. W., Moustakas J., Johnson-Groh M., 2015, *ApJ*, 806, A16
- Bertelli G., Bressan A., Chiosi C., Fagotto F., Nasi E., 1994, *A&AS*, 106, 275
- Bolatto A. D., Leroy A. K., Rosolowsky E., Walter F., Blitz L., 2008, *ApJ*, 686, 948
- Bresolin F., Kennicutt R. C., Jr, 1996, *ApJ*, 112, 1009
- Bresolin F., Kennicutt R. C., Garnett D. R., 1999, *ApJ*, 510, 104
- Bressan A., Marigo P., Girardi L., Salasnich B., Dal Cero C., Rubele S., Nanni A., 2012, *MNRAS*, 427, 127
- Brown R. L., Mathews W. G., 1970, *ApJ*, 160, 939
- Bruevich V. V., Gusev A. S., Ezhkova O. V., Sakhilov F. K., Smirnov M. A., 2007, *Astron. Rep.*, 51, 222
- Bruevich V. V., Gusev A. S., Guslyakova S. A., 2010, *Astron. Rep.*, 54, 375
- Bruevich V. V., Gusev A. S., Guslyakova S. A., 2011, *Astron. Rep.*, 55, 310
- Bruzual G., 2002, in Geisler D., Grebel E. K., Minniti D., eds *Proc. IAU Symp.* 207, *Extragalactic Star Clusters*. Astron. Soc. Pac., San Francisco, p. 166
- Calzetti D., 2001, *PASP*, 113, 1449
- Caplan J., Deharveng L., 1986, *A&A*, 155, 297
- Cedr s B., Cepa J., Bongiovanni  ., Casta eda H., S nchez-Portal M., Tomita A., 2012, *A&A*, 545, A43
- Cervi o M., 2013, *New Astron. Rev.*, 57, 123
- Chandar R. et al., 2010, *ApJ*, 719, 966
- Chen Y., Girardi L., Bressan A., Marigo P., Barbieri M., Kong X., 2014, *MNRAS*, 444, 2525
- Chen Y., Bressan A., Girardi L., Marigo P., Kong X., Lanza A., 2015, *MNRAS*, 452, 1068
- Copetti M. V. F., Pastoriza M. G., Dottori H. A., 1986, *A&A*, 156, 111
- Dale D. A. et al., 2009, *ApJ*, 703, 517
- de Grijs R., Anders P., 2006, *MNRAS*, 366, 295
- de la Fuente Marcos R., de la Fuente Marcos C., 2009, *ApJ*, 700, 436
- Efremov Y. N., 1989, *Sites of Star Formation in Galaxies: Star Complexes and Spiral Arms*. Fizmatlit, Moscow, p. 246 (in Russian)
- Efremov Y. N., 1995, *AJ*, 110, 2757
- Efremov Y. N., Elmegreen B., 1998, *MNRAS*, 299, 588
- Efremov Y. N., Ivanov G. R., Nikolov N. S., 1987, *Ap&SS*, 135, 119
- Efremov Y. N., Afanasiev V. L., Egorov O. V., 2011, *Astrophys. Bull.*, 66, 304
- Elmegreen B. G., 1994, *ApJ*, 433, 39
- Elmegreen B. G., 2002, *ApJ*, 564, 773

- Elmegreen B. G., 2009, in Andersen J., Bland-Hawthorn J., Nordström B., eds, Proc. IAU Symp. 254, The Galaxy Disk in Cosmological Context. Kluwer, Dordrecht, p. 289
- Elmegreen B. G., 2011, in Charbonnel C., Montmerle T., eds, EAS Publ. Ser. Vol. 51, Ecole Evry Schatzman 2010: Star Formation in the Local Universe. Cambridge Univ. Press, Cambridge, p. 31
- Elmegreen B. G., Efremov Y. N., 1996, *ApJ*, 466, 802
- Elmegreen B. G., Elmegreen D. M., Salzer J. J., Mann H., 1996, *ApJ*, 467, 579
- Elmegreen B. G., Efremov Y., Pudritz R. E., Zinnecker H., 2000, in Mannings V., Boss A. P., Russell S. S., eds, Protostars and Planets IV. Univ. Arizona Press, Tucson, AZ, p. 179
- Elmegreen B. G., Elmegreen D. M., Leitner S. N., 2003a, *ApJ*, 590, 271
- Elmegreen B. G., Leitner S. N., Elmegreen D. M., Cuillandre J.-C., 2003b, *ApJ*, 593, 333
- Elmegreen B. G., Elmegreen D. M., Chandar R., Whitmore B., Regan M., 2006, *ApJ*, 644, 879
- Elson R. A. W., Fall S. M., 1985, *ApJ*, 299, 211
- Emsellem E. et al., 2022, *A&A*, 659, A191
- Epinat B., Amram P., Marcelin M., 2008, *MNRAS*, 390, 466
- Ferguson A. M. N., Gallagher J. S., Wyse R. F. G., 1998, *AJ*, 116, 673
- Fouesneau M. et al., 2014, *ApJ*, 786, A117
- García-Benito R. et al., 2010, *MNRAS*, 408, 2234
- Gatto M. et al., 2021, *MNRAS*, 507, 3312
- Gieles M., Portegies Zwart S. F., 2011, *MNRAS*, 410, L6
- Girardi L., Bressan A., Bertelli G., Chiosi C., 2000, *A&AS*, 141, 371
- Gouliermis D. A. et al., 2017, *MNRAS*, 468, 509
- Groves B. et al., 2023, *MNRAS*, 520, 4902
- Grudić M. Y., Diederik Kruijssen J. M., Faucher-Giguère C.-A., Hopkins F., Ma X., Quataert E., Boylan-Kolchin M., 2021, *MNRAS*, 506, 3239
- Gusev A. S., 2006a, *Astron. Rep.*, 50, 167
- Gusev A. S., 2006b, *Astron. Rep.*, 50, 182
- Gusev A. S., Efremov Y. N., 2013, *MNRAS*, 434, 313
- Gusev A. S., Kaisin S. S., 2002, *Astron. Rep.*, 46, 712
- Gusev A. S., Kaisin S. S., 2004, *Astron. Rep.*, 48, 611
- Gusev A. S., Park M.-G., 2003, *A&A*, 410, 117
- Gusev A. S., Shimanovskaya E. V., 2019, *MNRAS*, 488, 3045
- Gusev A. S., Zasov A. V., Kaisin S. S., Bizyaev D. V., 2002, *Astron. Rep.*, 46, 704
- Gusev A. S., Zasov A. V., Kaisin S. S., 2003, *Astron. Lett.*, 29, 363
- Gusev A. S., Myakutin V. I., Sakhibov F. K., Smirnov M. A., 2007, *Astron. Rep.*, 51, 234
- Gusev A. S., Pilyugin L. S., Sakhibov F., Dodonov S. N., Ezhkova O. V., Khramtsova M. S., 2012, *MNRAS*, 424, 1930
- Gusev A. S., Sakhibov F. H., Dodonov S. N., 2013, *Astrophys. Bull.*, 68, 40
- Gusev A. S., Egorov O. V., Sakhibov F., 2014, *MNRAS*, 437, 1337
- Gusev A. S., Guslyakova S. A., Novikova A. P., Khramtsova M. S., Bruevich V. V., Ezhkova O. V., 2015, *Astron. Rep.*, 59, 899
- Gusev A. S. et al., 2016, *MNRAS*, 457, 3334
- Gusev A. S., Shimanovskaya E. V., Shatsky N. I., Sakhibov F., Piskunov A. E., Kharchenko N. V., 2018, *Open Astron.*, 27, 98
- Gusev A. S., Sakhibov F. Kh., Ezhkova O. V., 2020, *Astron. Rep.*, 64, 375
- Haas M. R., Gieles M., Scheepmaker R. A., Larsen S. S., Lamers H. J. G. L. M., 2008, *A&A*, 487, 937
- Hollyhead K., Bastian N., Adamo A., Silva-Villa E., Dale J., Ryon J. E., Gazak Z., 2015, *MNRAS*, 449, 1106
- Hollyhead K., Adamo A., Bastian N., Gieles M., Ryon J. E., 2016, *MNRAS*, 460, 2087
- Hopkins P. F., 2012, *MNRAS*, 423, 2016
- Ivanov G. R., 1991, *Ap&SS*, 178, 227
- James P. A. et al., 2004, *A&A*, 414, 23
- Kaplan S. A., Pikelner S. B., 1979, The Physics of the Interstellar Medium. Nauka, Moscow, p. 592 (in Russian)
- Kennicutt R. C., Jr, Lee J. C., Funes J. G. J. S., Sakai S., Akiyama S., 2008, *ApJS*, 178, 247
- Kharchenko N. V., Piskunov A. E., Röser S., Schilbach E., Scholz R.-D., 2005a, *A&A*, 438, 1163
- Kharchenko N. V., Piskunov A. E., Röser S., Schilbach E., Scholz R.-D., 2005b, *A&A*, 440, 403
- Kharchenko N. V., Piskunov A. E., Röser S., Schilbach E., Scholz R.-D., Zinnecker H., 2009, *A&A*, 504, 681
- Kim H. et al., 2012, *ApJ*, 753, A26
- Kim J. et al., 2021, *MNRAS*, 504, 487
- Kim J. et al., 2023, *ApJ*, 944, L20
- Knapen J. H., Stedman S., Bramich D. M., Folkes S. L., Bradley T. R., 2004, *A&A*, 426, 1135
- Konstantopoulos I. S., Bastian N., Smith L. J., Westmoquette M. S., Trancho G., Gallagher J. S., 2009, *ApJ*, 701, 1015
- Konstantopoulos I. S. et al., 2013, *AJ*, 145, A137
- Kreckel K. et al., 2022, *A&A*, 667, A16
- Lada C. J., Lada E. A., 2003, *ARA&A*, 41, 57
- Lang K. R., 1978, Astrophysical Formulae. A Compendium for the Physicist and Astrophysicist. Springer-Verlag, Berlin, Heidelberg, New York, p. 783
- Larsen S. S., 2002, *AJ*, 124, 1393
- Larsen S. S., Richtler T., 1999, *A&A*, 345, 59
- Larson R. B., 1981, *MNRAS*, 194, 809
- Larson K. L. et al., 2023, *MNRAS*, 523, 6061
- Lee J. C. et al., 2022, *ApJS*, 258, A10
- Leitherer C. et al., 1999, *ApJS*, 123, 3
- McCall M. L., Rybski P. M., Shields G. A., 1985, *ApJS*, 57, 1
- Marigo P., Girardi L., 2007, *A&A*, 469, 239
- Marigo P., Girardi L., Bressan A., Groenewegen M. A. T., Silva L., Granato G. L., 2008, *A&A*, 482, 883
- Marino R. A. et al., 2013, *A&A*, 559, A114
- Messa M. et al., 2018, *MNRAS*, 473, 996
- Mora M. D., Larsen S. S., Kissler-Patig M., Brodie J. P., Richtler T., 2009, *A&A*, 501, 949
- Morisset C. et al., 2016, *A&A*, 594, A37
- Odekun M. C., 2008, *ApJ*, 681, 1248
- Osterbrock D. E., 1989, Astrophysics of Gaseous Nebulae and Active Galactic Nuclei. University Science Books, Mill Valley, CA, p. 422
- Patrel G., Petit C., Prugniel Ph., Theureau G., Rousseau J., Brouty M., Dubois P., Cambresy L., 2003, *A&A*, 412, 45
- Pérez-Montero E., 2014, *MNRAS*, 441, 2663
- Pettini M., Pagel B. E. J., 2004, *MNRAS*, 348, L59
- Pilyugin L. S., Grebel E. K., 2016, *MNRAS*, 457, 3678
- Pilyugin L. S., Mattsson L., 2011, *MNRAS*, 412, 1145
- Pilyugin L. S., Grebel E. K., Kniazev A. Y., 2014, *AJ*, 147, A131
- Piskunov A. E., Kharchenko N. V., Röser S., Schilbach E., Scholz R.-D., 2006, *A&A*, 445, 545
- Piskunov A. E., Kharchenko N. V., Schilbach E., Röser S., Scholz R.-D., Zinnecker H., 2011, *A&A*, 525, 122
- Popescu B., Hanson M. M., Elmegreen B. G., 2012, *ApJ*, 751, A122
- Portegies Zwart S. F., McMillan S. L. W., Gieles M., 2010, *ARA&A*, 48, 431
- Regan M. W. et al., 2004, *ApJS*, 154, 204
- Reines A. E., Nidever D. L., Whelan D. G., Johnson K. E., 2010, *ApJ*, 708, 26
- Rosales-Ortega F. F., Diaz A. I., Kennicutt R. C., Sanchez S. F., 2011, *MNRAS*, 415, 2439
- Rosolowsky E. et al., 2021, *MNRAS*, 502, 1218
- Ryon J. E. et al., 2015, *MNRAS*, 452, 525
- Ryon J. E. et al., 2017, *ApJ*, 841, A92
- Sakhibov F., Smirnov M. A., 1990, *Sov. Astron.*, 34, 236
- Sakhibov F., Smirnov M. A., 1995, *Astron. Rep.*, 39, 281
- Sánchez S. F. et al., 2012, *A&A*, 546, A2
- Santoro F. et al., 2022, *A&A*, 658, A188
- Scalo J. M., 1986, Fundamentals of Cosmic Physics. Vol. 11, Gordon and Breach, Science Publishers, Inc., New York, p. 1
- Scheuermann F. et al., 2023, *MNRAS*, 522, 2369
- Searle L., Wilkinson A., Bagnuolo W. G., 1980, *ApJ*, 239, 803
- Tang J., Bressan A., Rosenfield P., Slemmer A., Marigo P., Girardi L., Bianchi L., 2014, *MNRAS*, 445, 4287
- Thilker D. A. et al., 2022, *MNRAS*, 509, 4094
- Turner J. A. et al., 2021, *MNRAS*, 502, 1366

- van Zee L., Salzer J. J., Haynes M. P., O'Donoghue A. A., Balonek T. J., 1998, *AJ*, 116, 2805
- Wei L. H., Keto E., Ho L. C., 2012, *ApJ*, 750, 136
- Whitmore B. C. et al., 2010, *AJ*, 140, 75
- Whitmore B. C. et al., 2011, *ApJ*, 729, 78
- Whitmore B. C. et al., 2021, *MNRAS*, 506, 5294
- Wofford A., Leitherer C., Chandar R., 2011, *ApJ*, 727, A100
- Young J. S., Allen L., Kenney J. D. P., Lesser A., Rownd B., 1996, *AJ*, 112, 1903
- Zhang Q., Fall S. M., Whitmore B. C., 2001, *ApJ*, 561, 727

SUPPORTING INFORMATION

Supplementary data are available at [MNRAS](#) online.

Please note: Oxford University Press is not responsible for the content or functionality of any supporting materials supplied by the authors. Any queries (other than missing material) should be directed to the corresponding author for the article.

This paper has been typeset from a $\text{\TeX}/\text{\LaTeX}$ file prepared by the author.